



**HAL**  
open science

## Understanding the West African Monsoon from the analysis of diabatic heating distributions as simulated by climate models

Gill Martin, P. Peyrillé, R. Roehrig, Catherine Rio, M. Caian, Gilles Bellon, Francis Codron, Jean-Philippe Lafore, D. E. Poan, Abderrahmane Idelkadi

### ► To cite this version:

Gill Martin, P. Peyrillé, R. Roehrig, Catherine Rio, M. Caian, et al.. Understanding the West African Monsoon from the analysis of diabatic heating distributions as simulated by climate models. *Journal of Advances in Modeling Earth Systems*, 2017, 70, pp.1297 - 1297. 10.1002/2016MS000697 . hal-01507050

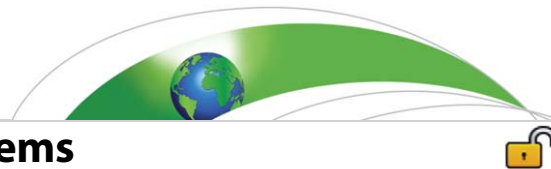
**HAL Id: hal-01507050**

**<https://hal.science/hal-01507050>**

Submitted on 12 Apr 2017

**HAL** is a multi-disciplinary open access archive for the deposit and dissemination of scientific research documents, whether they are published or not. The documents may come from teaching and research institutions in France or abroad, or from public or private research centers.

L'archive ouverte pluridisciplinaire **HAL**, est destinée au dépôt et à la diffusion de documents scientifiques de niveau recherche, publiés ou non, émanant des établissements d'enseignement et de recherche français ou étrangers, des laboratoires publics ou privés.



## RESEARCH ARTICLE

10.1002/2016MS000697

# Understanding the West African Monsoon from the analysis of diabatic heating distributions as simulated by climate models

G. M. Martin <sup>1</sup>, P. Peyrillé<sup>2</sup>, R. Roehrig <sup>2</sup>, C. Rio<sup>3</sup>, M. Caian<sup>4</sup>, G. Bellon <sup>2,5</sup>, F. Codron <sup>3</sup>, J.-P. Lafore<sup>2</sup>, D. E. Poan<sup>2,6</sup>, and A. Idelkadi<sup>3</sup>

### Key Points:

- Diabatic components in the West African Monsoon (WAM) region are available from four model families with different physical packages
- Analysis of these diabatic components gives insight into the processes influencing the WAM and indicates where model development is needed
- Radiative heating in the Sahara and the representation of clouds and convection in the rainband and Sahel are key for the WAM circulation

### Supporting Information:

- Supporting Information S1
- Table S1
- Table S2

### Correspondence to:

G. Martin,  
gill.martin@metoffice.gov.uk

### Citation:

Martin, G. M., P. Peyrillé, R. Roehrig, C. Rio, M. Caian, G. Bellon, F. Codron, J.-P. Lafore, D. E. Poan, and A. Idelkadi (2017), Understanding the West African Monsoon from the analysis of diabatic heating distributions as simulated by climate models, *J. Adv. Model. Earth Syst.*, 9, doi:10.1002/2016MS000697.

Received 21 APR 2016

Accepted 4 DEC 2016

Accepted article online 20 DEC 2016

© 2016. The Authors.

This is an open access article under the terms of the Creative Commons Attribution-NonCommercial-NoDerivs License, which permits use and distribution in any medium, provided the original work is properly cited, the use is non-commercial and no modifications or adaptations are made.

<sup>1</sup>Met Office Hadley Centre, Exeter, UK, <sup>2</sup>Centre National de Recherches Météorologiques, Météo-France and CNRS, Toulouse, France, <sup>3</sup>Laboratoire de Météorologie Dynamique, Institut Pierre-Simon Laplace, Paris, France, <sup>4</sup>Rosby Centre, Swedish Meteorological and Hydrological Institute, Norrköping, Sweden, <sup>5</sup>Now at Department of Physics, University of Auckland, New Zealand, <sup>6</sup>Now at Canadian Network for Regional Climate and Weather Processes, Université du Québec, Montréal, Canada

**Abstract** Vertical and horizontal distributions of diabatic heating in the West African monsoon (WAM) region as simulated by four model families are analyzed in order to assess the physical processes that affect the WAM circulation. For each model family, atmosphere-only runs of their CMIP5 configurations are compared with more recent configurations which are on the development path toward CMIP6. The various configurations of these models exhibit significant differences in their heating/moistening profiles, related to the different representation of physical processes such as boundary layer mixing, convection, large-scale condensation and radiative heating/cooling. There are also significant differences in the models' simulation of WAM rainfall patterns and circulations. The weaker the radiative cooling in the Saharan region, the larger the ascent in the rainband and the more intense the monsoon flow, while the latitude of the rainband is related to heating in the Gulf of Guinea region and on the northern side of the Saharan heat low. Overall, this work illustrates the difficulty experienced by current climate models in representing the characteristics of monsoon systems, but also that we can still use them to understand the interactions between local subgrid physical processes and the WAM circulation. Moreover, our conclusions regarding the relationship between errors in the large-scale circulation of the WAM and the structure of the heating by small-scale processes will motivate future studies and model development.

## 1. Introduction

Monsoon systems represent the dominant variation in the climate of the tropics with profound local, regional, and global impacts. Over half of the world's population, mostly in developing countries, lives under the influence of monsoon-dominated climates. The West African monsoon (WAM) has been the focus of a considerable volume of research over the past decade. Projects such as the African Monsoon Multidisciplinary Analysis programme (AMMA) [see Redelsperger *et al.*, 2006] have improved our understanding of key WAM features [Lafore *et al.*, 2010, 2011]. However, many of the current generation of climate models struggle to capture the major features of the WAM climatology and variability [e.g., Hourdin *et al.*, 2010; Roehrig *et al.*, 2013]. Roehrig *et al.* [2013] carried out a process-oriented analysis of the WAM in the Fifth Coupled Model Intercomparison Project (CMIP5) set of multimodel simulations. Significant errors in the WAM simulation were highlighted by that study, including the cloud radiative effects and the overall radiative budget. However, those authors also pointed that it remains difficult to draw conclusions on the causes of model deficiencies among a large set of simulations without sensitivity experiments.

In the tropics, the diabatic heating is the main source of energy that drives the atmospheric circulation. The tropical region receives two-thirds of the global rainfall, and the associated latent heat release forms the dominant part of the diabatic heating. The large-scale tropical circulation is found to be significantly influenced by the vertical distribution of the latent heat [e.g., Lau and Peng, 1987; Schumacher *et al.*, 2004]. The circulation then feeds back on the diabatic heating through atmospheric instabilities. Nonlatent heating processes (such as surface sensible heating and radiation) also play an important role.

Previous studies have investigated the role of different sources of diabatic heating on the WAM. For example, Hagos and Zhang [2010] showed that moisture transport within the near-surface circulation driven by the

heating gradient between the Sahara and the Gulf of Guinea counteracts the advection of dry air from the north by the latent heating driven deep circulation converging in the monsoon rainband, thereby influencing the seasonal advance of the WAM. *Poan et al.* [2014] gave a first description of the diabatic heating and moistening associated with African Easterly Waves (AEWs) using reanalyses. They showed that the meridional distribution of diabatic heating and moistening varies considerably through the AEW life cycle and that the resulting modification of the meridional heating gradients induces changes in the WAM circulation. *Peyrillé et al.* [2016] used an idealized meridional-vertical numerical model forced by heating and moistening derived from reanalyses to demonstrate that advection by the shallow meridional circulation (SMC) between the rainband and the Sahara largely determines the location and extent of the WAM rainband, while the annual cycle and spatial pattern of rainfall are influenced by the processes contributing to convective heating and drying.

The studies mentioned above have provided insight into the processes acting within the WAM. However, while the spatial distribution of heating and moistening has been analyzed with reanalyses or within an idealized model, previous studies have not had the opportunity to examine the WAM using models from which the details of the different process contributions to the heating and moistening have been available. In the present study, for the first time, the individual contributions from physical parameterizations to the diabatic heating components and their horizontal and vertical distribution in the WAM region have been collected from four different model families: LMDZ models from the Laboratoire de Météorologie Dynamique (LMD) of the Institut Pierre-Simon Laplace (IPSL) Paris; ARPEGE-Climat models from the Centre National de Recherches Météorologiques (CNRM) of Météo-France and CNRS; MetUM from Met Office UK, and EC-Earth models from the Swedish Meteorological and Hydrological Institute (SMHI), Sweden. Each of these modeling centers was a partner in the Earth system Model Bias Reduction and assessing Abrupt Climate Change (EMBRACE) project (under the European Commission's 7th Framework Programme), whose aim was to improve the representation of critical processes in climate and Earth System Models. For each model family, atmosphere-only runs of their CMIP5 configurations have been analyzed, along with more recent configurations which include both parameterization changes resulting from work done within the EMBRACE project and those ensuing from ongoing model development. Updates include changes to turbulent mixing, convective entrainment, convection closure and triggering, deep convection/large-scale partitioning, cloud schemes, aerosols, surface albedo, and surface hydrology.

The aim of our work is to use this set of model realizations to improve our understanding of the WAM system, the processes involved in it and how they are balanced with the WAM dynamics. The questions we wish to address with this study are:

1. What can we learn from this variety of realizations in terms of important processes that influence the WAM features/circulation?
2. How do different heating and moistening characteristics contribute to the differences between the model simulations of the WAM mean state?
3. Can the influence of changes within model families on the WAM circulation provide any guidance for future model development?

We analyze the WAM system as represented in the participating models and observations/reanalyses, and use the spread of their WAM representation to investigate the relationship between WAM key features (section 3). In section 4, we analyze the distribution of the diabatic components across the meridional transect. Using a few hypotheses, we then derive in each model the circulation balancing the heating distribution and examine its consistency with the simulated circulation. The contributions to the total diabatic heating from the different physical parameterizations are then further assessed to gain insight in the understanding of model differences. In section 5, we investigate the relationships between key features of the WAM and different parts of the heating distribution, thereby providing insight into the physical processes which might be instrumental in the way forward for climate model improvements in the context of the WAM system. Section 6 summarizes the findings and provides motivation for further work using this unique data set; finally, our conclusions are presented in section 7.

## 2. Data and Methods

### 2.1. Model Configurations and Experiments

The models used are all atmosphere-only configurations. Each was run for a minimum of 10 years in a period representative of the present day (between 1979 and 2009), following the AMIP protocol proposed in

**Table 1.** List of Model Experiments and Naming Conventions Used in This Study

Center	Model Configurations	Naming Conventions	Model Years Used
Met Office, UK	MetUM HadGEM2-A, used in CMIP5	HadGEM2-A (HG2-A)	1979–2008
	Prototype GA7 (a development configuration between Global Atmosphere v6 (GA6) and GA7, officially labeled as GA6.0#136.5)	ProtoGA7	1989–2008
LMD, IPSL Paris	LMDZ5A, used in CMIP5	LMDZ5A	1990–1999
	LMDZ5B (used to produce a subset of CMIP5 simulations with IPSL-CM5B)	LMDZ5B	1990–1999
	NPv4.12bis (a development configuration)	NPv4.12bis	1982–1989
	NPv4.12.OR11: NPv4.12bis plus new hydrology for soil scheme	NPv4.12.OR11	1982–1989
CNRM, Météo-France, Toulouse	ARPEGE-Climat V5.2, used in CMIP5	CNRM-AM5	1999–2008
	PreCNRM-AM6 (a development configuration, based on ARPEGE-Climat V6.1)	PreCNRM-AM6	1999–2008
SMHI, Sweden	EC-Earth v2.3, used in CMIP5	EC-Earth v2.3	1980–2009
	EC-Earth v3.1 (new configuration)	EC-Earth v3.1 Ctrl	1980–2009
	EC-Earth v3.1 CPB (including new CAPE closure for deep convection)	EC-Earth v3.1 CPB	1980–2009

CMIP5 [Taylor et al., 2012], in particular regarding forcings for sea surface temperature and sea ice extent. Monthly mean increments to temperature and moisture from each of the models' physical parameterizations were output and climatological means for each month were created. The model runs and naming conventions used in this paper are shown in Table 1. Details of the different model configurations as used in CMIP5 are given in the supporting information Table S1. Since CMIP5, changes have been made within each model family as part of on-going model development at each modeling center and stimulated by the EMBRACE project framework. Supporting information Table S2 shows the new (prototype) model configurations examined in our study. Significant differences from the previous configuration of each model are highlighted in bold, and further details on the major changes in each model family are given in the supporting information. It is important to note that none of these newer configurations represents a final model setup and further work will be required at each modeling center before the configurations are officially released for CMIP6. However, they are used in the present study in order to investigate the influence of significant diabatic heating changes on the monsoon simulations.

In subsequent sections, comparisons are made against reanalyses [ERA-Interim, Simmons et al., 2007; MERRA, Rienecker et al., 2011], CERES-EBAF satellite radiances [Loeb et al., 2009], and observed precipitation data sets [CMAP: Xie and Arkin, 1997; GPCP2: Huffman et al., 2001; TRMM-3B42: Huffman et al., 2007].

## 2.2. Definitions of Diabatic Terms

Diabatic heating and drying, or the apparent heat source  $Q_1$  and apparent moist sink  $Q_2$ , were defined by Yanai et al. [1973] in their study of tropical cloud clusters. They used this approach to explain how the large amount of latent heat liberated in deep convection affects the heat and moisture budgets of the large-scale environment. The total diabatic heating,  $Q_1$ , is the sum of latent heating, radiative heating, and turbulent mixing of heat. The total diabatic drying,  $Q_2$ , is the sum of the net condensation and the vertical divergence of the vertical turbulent transport of moisture.

The diabatic heating associated with the monsoon precipitation represents an important forcing to the global atmospheric circulation. Several studies have concluded that a realistic vertical and horizontal distribution of heating is critical for accurate representation of tropical precipitation and its variability [e.g., Hoskins and Rodwell, 1995; Lin, 2009; Lappen and Schumacher, 2012; Stachnik et al., 2013]. The simulation of vertical and horizontal heating distributions by large-scale models is directly linked to the methods the models use to represent cloud and precipitation processes.

In models, the diabatic terms are each derived by summing the temperature and moisture increments from the different physical schemes. The moisture increments are then multiplied by the latent heat of condensation to derive the apparent heat source due to moisture sinks. The diabatic terms for the MERRA reanalyses are derived in the same way, but for ERA-Interim reanalyses, they are computed as residuals ("res" superscript) of the 6 hourly energy and moisture budget [e.g., Poan et al., 2014]. By construction, budgets are closed, and any errors come from reanalysis and discretization errors.

In section 4.3, column-integrated budgets are considered for  $Q_1$ ,  $Q_2$ , and  $Q_1-Q_2$ . These are denoted by  $\langle Q_1 \rangle$ ,  $\langle Q_2 \rangle$ , and  $\langle Q_1-Q_2 \rangle$ . Their calculation method is described in Appendix C.

### 2.3. Relating the Diabatic Heating to the WAM Circulation

It is tempting when analyzing the spatial distribution of  $Q_1$  to relate it to the atmospheric circulation. *Hagos and Zhang* [2010] derived a diagnostic divergent circulation from  $Q_1$  in different reanalyses and showed that moisture convergence is driven by the Saharan Heat Low (SHL) heating. *Kim and Lee* [2001] proposed a linear diagnostic of the quasi-geostrophic meridional circulation to analyze the response of the mean meridional Hadley cell to a specific source of heating. It is beyond the scope of this paper to analyze the response of each contribution, but it remains insightful to compare an estimate of the axisymmetric circulation that would balance the mean meridional distribution of  $Q_1$ , namely a mean nondivergent meridional stream function noted  $\overline{\psi_{diab}^{nd}}$ , with the zonal mean nondivergent stream function,  $\overline{\psi^{nd}}$ . The aim is not to attribute a specific change in the circulation to a change in  $Q_1$ , which would require either specific model sensitivity experiments or a more complex framework, but rather to analyze how consistent the climatological nondivergent meridional circulation and  $Q_1$  are among this set of model simulations.

Details on the calculation of  $\overline{\psi^{nd}}$  and  $\overline{\psi_{diab}^{nd}}$  are given in Appendix A. The diagnostic circulation is based on the neglect of horizontal advections in the temperature equation (often called the Weak Temperature Gradient (WTG) approximations) and on the assumption of mass conservation in the  $(y, z)$  plane. The latter assumption is well verified over West Africa (see Appendix B), which shows that understanding the zonal mean structure of the WAM is a first order step to be achieved. The former works well mainly in the free troposphere.

A good agreement between  $\overline{\psi_{diab}^{nd}}$  and  $\overline{\psi^{nd}}$  is expected within the deep tropics, where horizontal gradients of temperature are weak, but the situation is not straightforward over Africa since nonlinearity arising from synoptic transients is likely to play a crucial role in the WAM circulation [*Poan et al.*, 2013]. In addition, disagreement between the two stream functions may indicate adjustments of the meridional circulation by three-dimensional effects, such as zonal divergence of mass [*Peyrillé et al.*, 2016].

## 3. Meridional Characteristics of the WAM Region

### 3.1. Basic Features of the WAM

The WAM presents a strong zonal symmetry especially over West Africa due to the orientation of the coast at  $\sim 5^\circ\text{N}$  nearly parallel to the Equator between  $10^\circ\text{W}$  and  $10^\circ\text{E}$ . This convenient property allows analysis of the mean meridional vertical cross section between the above longitudes and has been often used to evaluate models in the region [e.g., *Hourdin et al.*, 2010; *Roehrig et al.*, 2013]. *Lafore et al.* [2010] introduces the main features of the WAM, which will be extensively used in the discussion below:

1. The primary driving mechanism for the seasonal migration of the WAM over the continent is the evolution of the thermal contrast between the summer heating of African continent and spring cooling of the Gulf of Guinea through the Atlantic cold tongue [*Sultan and Janicot*, 2003; *Caniaux et al.*, 2011]. On a broader scale, the radiative deficit in midlatitudes compared with the excess of moist static energy within the tropics drives the deep meridional circulation.
2. Latent heating in the monsoon rainband associated with convective processes thus drives a deep circulation and corresponding moisture convergence into the region of precipitation, while also inducing low-level dry air advection from the north. This region is defined as the ITCZ.
3. The SHL corresponds to a shallow but well-developed dry-convective atmospheric boundary layer. Heating by sensible heat fluxes and radiation is influenced here by the concentration and optical properties of aerosols and high-level clouds, as well as the Saharan surface albedo. In the free troposphere, radiative cooling prevails over the SHL associated with dry air and large-scale subsidence.
4. The SHL pressure minimum and the meridional gradient in surface sensible heat flux drives the convergence of two opposing low-level flows along the Inter-Tropical Discontinuity ITD: the northerly dry and hot flow (continental trade wind) and the southwesterly moist and cooler monsoon flow. This transports moisture at low levels far into the continent, promoting the northward migration of monsoon precipitation [*Hagos and Zhang*, 2010].
5. The SMC is associated with subsiding air over the Gulf of Guinea, a shallow moist boundary layer and low-level moisture divergence.

6. The resulting strong baroclinicity south of the ITD in the Sahel band [10°N–20°N], together with associated contrasts in convection (moist to the south and dry to the north; *Thorncroft and Blackburn* [1999]), is responsible for the midlevel African Easterly Jet AEJ, with its core located around 600 hPa.
7. Deep convection occurs in the ITCZ on the southern flank of the AEJ, where rainfall is maximum, with a secondary maximum north of the coast.
8. At upper levels we have the Tropical Easterly Jet (TEJ) corresponding to the upper branch of the Walker cell initiated by the Indian Monsoon. The convective outflow tends to accelerate the TEJ over Africa.

Meridional cross sections of the aforementioned quantities from the models and reanalyses/observations are shown in Figures 1–3 and discussed in the next section.

### 3.2. Climate Model Representation of Main WAM Features

The meridional distributions of rainfall (Figures 1a and 1b) illustrate the spread in the average position and intensity of the WAM rainband across the set of model simulations. In CNRM-AM5 and EC-Earth v2.3, the rainband is displaced northward. This is associated with high precipitable water for CNRM-AM5 and low precipitable water for EC-Earth v2.3 (Figure 1c), highlighting different convective precipitation efficiency. The latitudinal distribution of rain is improved in CMIP6 prototypes, although the amount of rainfall in PreCNRM-AM6 is particularly excessive and that from ProtoGA7 is particularly small. The strength and position of the SHL varies between the models (as can be seen from the mean sea level pressure shown in Figures 1e and 1f), and corresponds to various shapes of the meridional gradient of potential temperature ( $\theta$ ); Figures 1g and 1h). This is consistent with the variations in the position of the ITD (where the meridional wind at 925 hPa changes sign in Figures 2a and 2c) and of the AEJ (maximum of zonal wind at 600 hPa in Figures 2b and 2d), the location of the rainfall maximum (Figures 1a and 1b) and the precipitable water content (Figures 1c and 1d). Some of these relationships are explored further in section 3.3.

Variations in  $\theta$  at 925 hPa over the Gulf of Guinea (Figures 1g and 1h) are associated with variable amounts and heights of low-level cloud in this region. This is confirmed by the meridional distribution of radiation heating at the surface and top of atmosphere (TOA) shown in Figure 3. Low-level clouds reflect SW radiation, reducing the net incoming SW at both the surface and the TOA in the full-sky fluxes compared with those from clear-sky only (dashed lines in Figure 3). Similarly, variations in  $\theta_{925}$  and  $\theta_{850}$  over the Sahara are associated with differences in radiative heating here: the presence of aerosols and the desert high surface albedo reduce the net incoming SW at TOA, while the high surface temperatures are associated with large outgoing LW fluxes. In the main rainband region (7°N–12°N), deep convective clouds reduce the net incoming SW and outgoing LW at the TOA, as well as decreasing the net incoming SW at the surface.

The models capture the first order of the observed radiative fluxes, although CNRM-AM5 stands out with excessive incoming SW at the TOA and weak incoming SW at the surface over the Sahara, and excessive incoming SW at the surface and TOA over the Gulf of Guinea. Over the latter region, CNRM-AM5 has almost the same values for clear-sky and full-sky, indicating a lack of stratocumulus clouds. In contrast, HadGEM2-A and LMDZ5B underestimate the total incoming SW in this region, suggesting too much low-level cloud cover. Almost all of the model configurations overestimate the outgoing LW at TOA in the WAM rainband, consistently with their systematic underestimate of the rainfall amount. CNRM-AM5 and EC-Earthv2.3 also underestimate the incoming SW at the surface in the rainband region and the Sahel, consistent with their northward displacement of the rainband. The improved representation cloud radiative effects between 0°N and 10°N in the LMDZ family of models comes both from the activation of the thermal plume model for dry and shallow convection and from the activation of a new statistical bi-Gaussian scheme to represent shallow clouds (see supporting information S1.3).

As mentioned above, PreCNRM-AM6 stands out as having excessive rainfall in the rainband compared with the other model configurations and the observations. This model configuration includes a Prognostic Condensate Microphysics Transport (PCMT) scheme (see supporting information S1.1) which alters the balance between large-scale and convective precipitation significantly. ProtoGA7 also includes a change to a prognostic cloud and condensate scheme (PC2; see supporting information S1.2), but in this case the amount of rainfall is reduced (Figures 1a and 1b) and the PMSL gradient and the position of the rainband remain similar to that in HadGEM2-A; this may point to larger-scale feedbacks in this model which maintain the rainband at 10°N. The decrease in rainfall north of 5°N in LMDZ5B compared with LMDZ5A is due to the activation of a convective entrainment more sensitive to tropospheric humidity (see supporting information

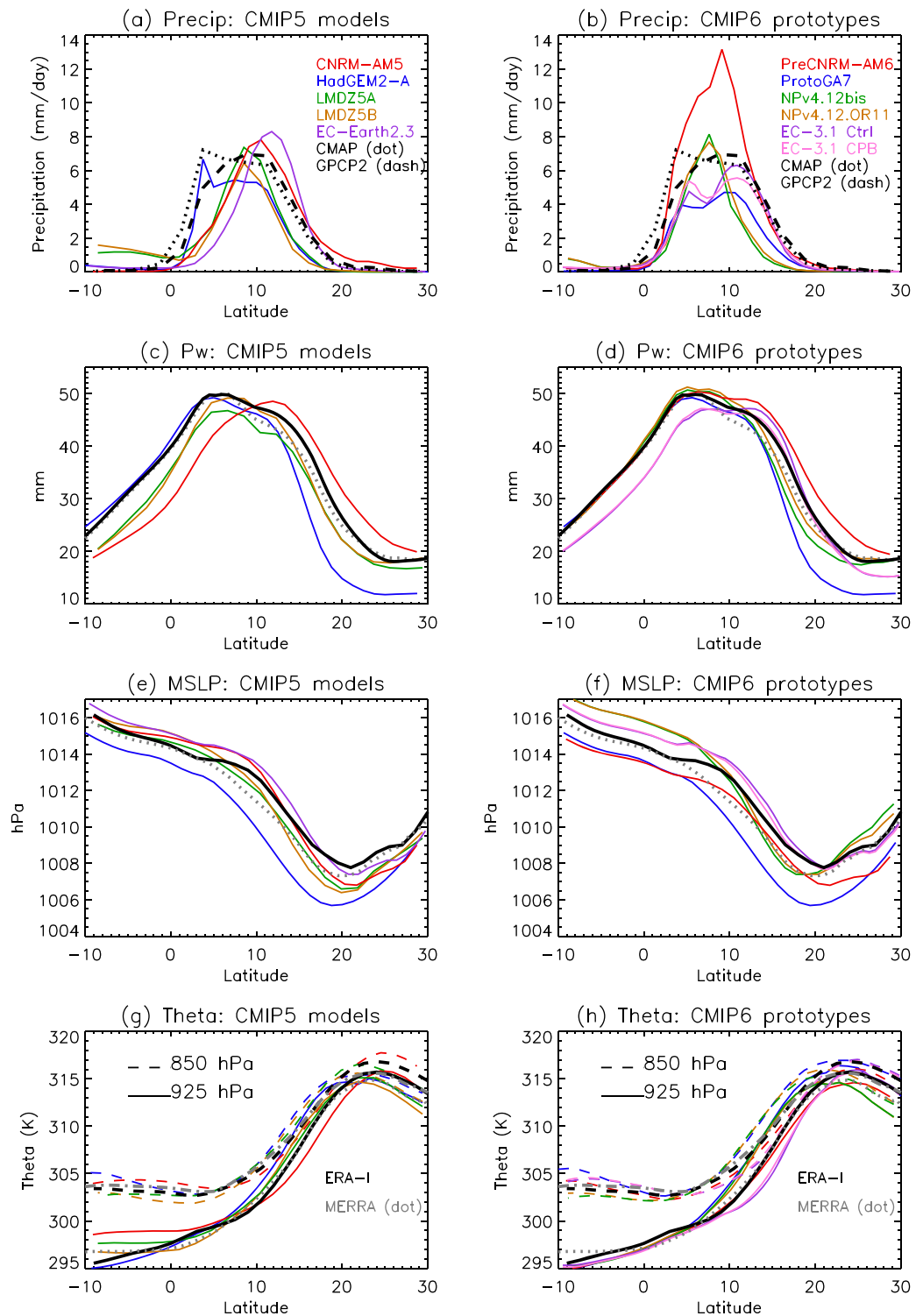


**Figure 1.** Latitudinal cross sections of surface fields in the WAM region (10°W to 10°E) in JJA, for the (left) CMIP5 configurations and (right) CMIP6 prototypes and from MERRA and ERA-I reanalyses and CMAP and GPCP2 observations. Precip: precipitation; Pw: precipitable water content; MSLP: mean sea level pressure; Theta: potential temperature ( $\theta$ ). Note that precipitable water content was not available for EC-Earthv2.3.

S1.3) and is associated with an increase of precipitable water, suggesting weaker precipitation efficiency by the modified convection scheme in this configuration. This change is enhanced in NPv4.12bis and NPv4.12.OR11 in which the parameter controlling maximum precipitation efficiency has been decreased.

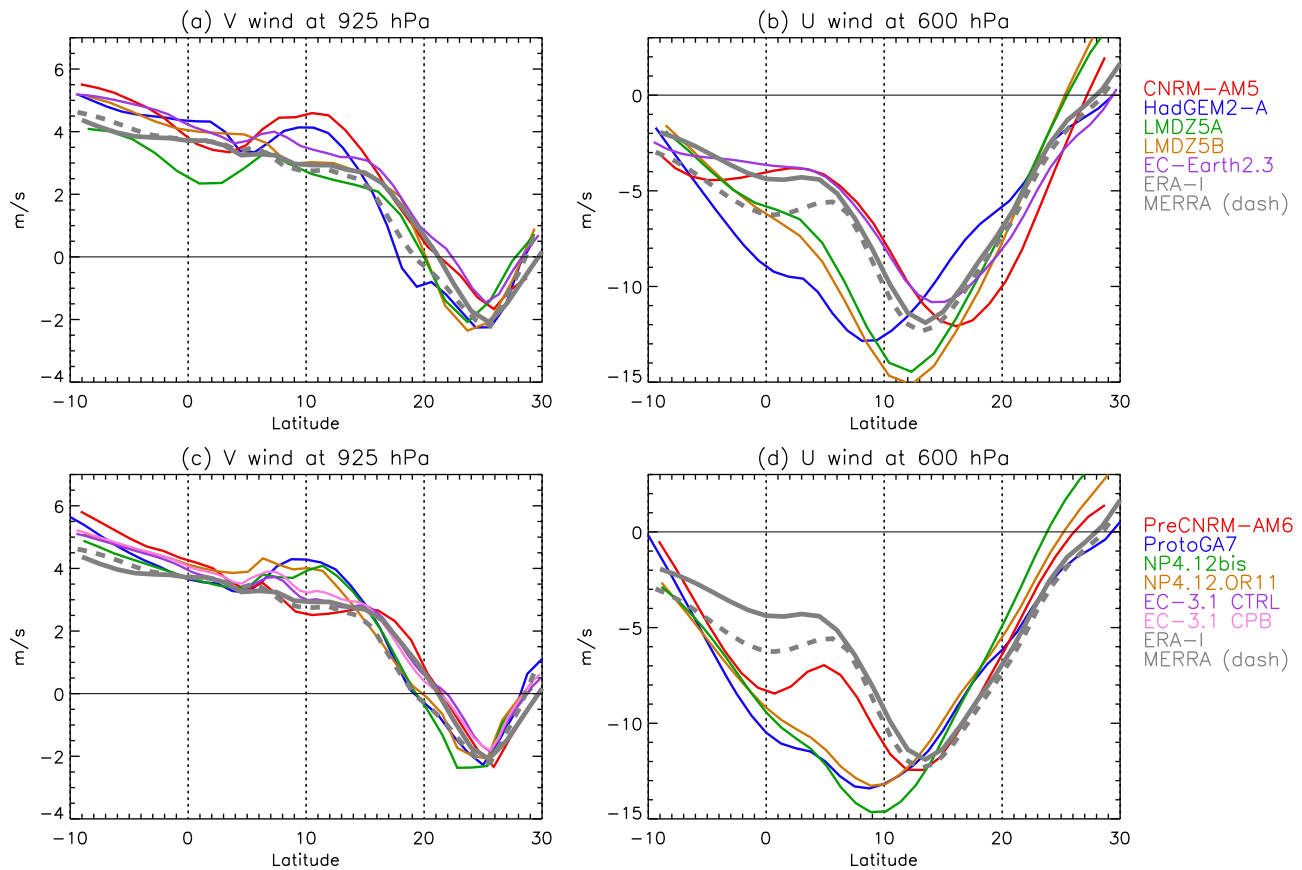


**Figure 2.** Wind cross sections between 10W-10E in the different model configurations in JJA. (a and c) Meridional winds at 925 hPa; (b and d) zonal wind at 600 hPa. Units:  $\text{m s}^{-1}$ .

The change to the convection parameterization in NPv4.12bis is also associated with a southward shift of rainfall, which was already too far south in LMDZ5B (Figures 1a and 1b). Precipitation is suppressed over the ocean, while precipitation along the coast is increased. This might be related to the activation of the thermal plume model in regions of strong inversion (such as over the Gulf of Guinea) in NPv4.12. In contrast, changes in the convection scheme in EC-Earthv3.1 CPB (see supporting information S1.4), which are mainly linked to convection onset timing over land areas (delayed and closer to observations in EC-Earthv3.1 CPB), do not significantly change the model response. However, these changes do lead to energy balance changes and have an impact on both regional (e.g., precipitation in the WAM rainband) and large-scale circulation features (a slight northward shift and strength decrease in AEJ).

It is clear from this discussion that changes to the models' representation of clouds and convection have a strong influence on their simulation of the WAM.

### 3.3. Relationships Between Key Features of the WAM

We now examine relationships between a few key features of the WAM system. Figure 4 shows scatterplots that indicate that the meridional potential temperature gradient between the Saharan and Gulf of Guinea region is clearly related to the ITD latitude, with a stronger temperature gradient promoting greater northward penetration of the low-level flow. There is a weaker, but still positive, relationship with the latitude of maximum rainfall in the rainband, while the relationship between the ITCZ peak and ITD latitudes itself is strong. These relationships are consistent with our understanding of the WAM system [e.g., Lafore *et al.*, 2010] and Figure 4 illustrates that the models are able to capture them, albeit with considerable spread even between the values from reanalyses/observations. It should be noted that there is no direct pairing between the values from the two reanalyses and the two satellites observed rainfall estimates; therefore, the four cross pairings between these are shown in Figure 4 for reference only and their values are not included in the linear regressions.

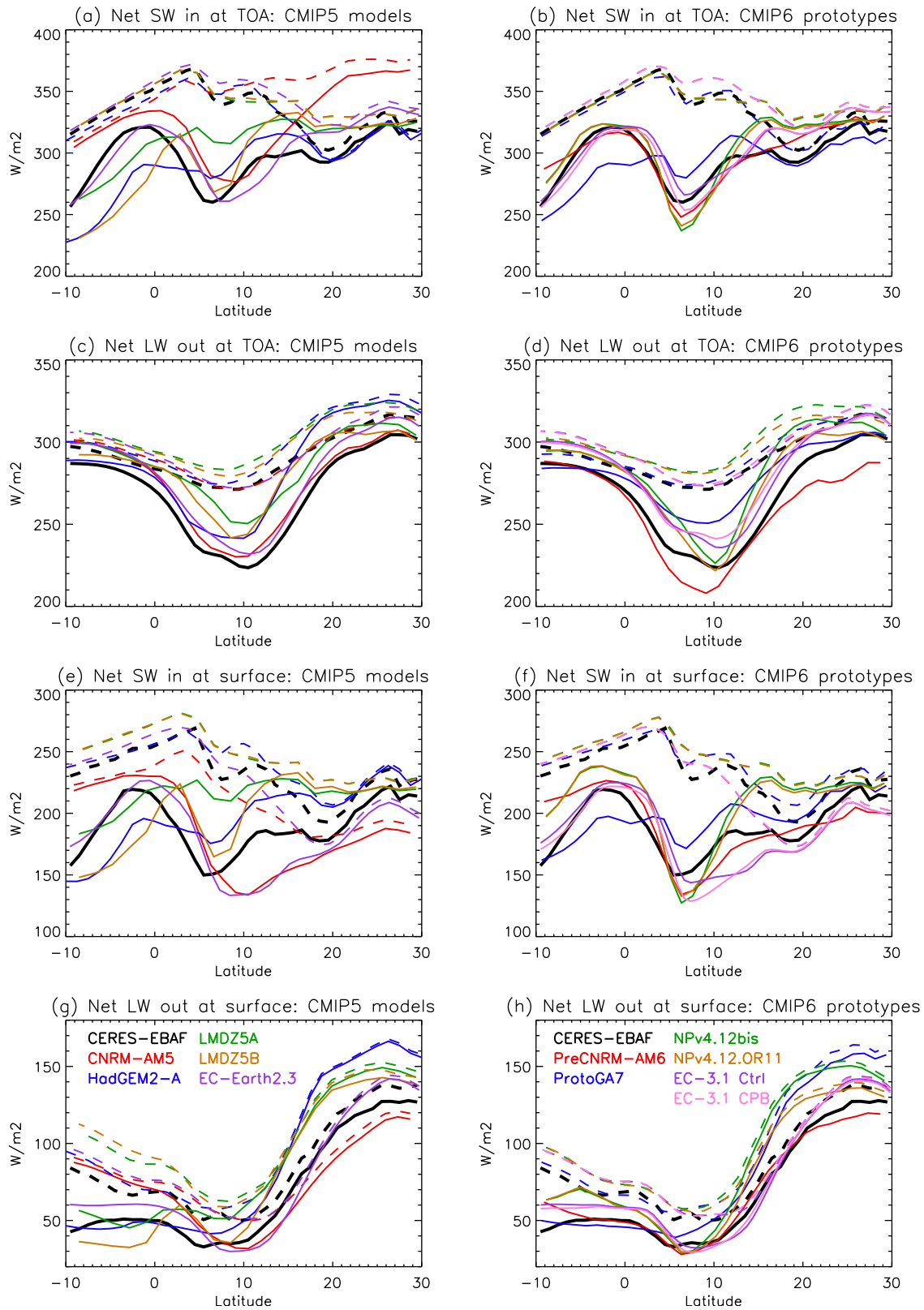


**Figure 3.** Latitudinal cross sections of radiation components at top of atmosphere (TOA) and surface in JJA in the WAM region (10°W to 10°E) for the CMIP5 model configurations, the prototype-CMIP6 configurations and for CERES-EBAF satellite observations [Loeb *et al.*, 2009]. Full (solid) and clear-sky only (dashed) are shown where available.

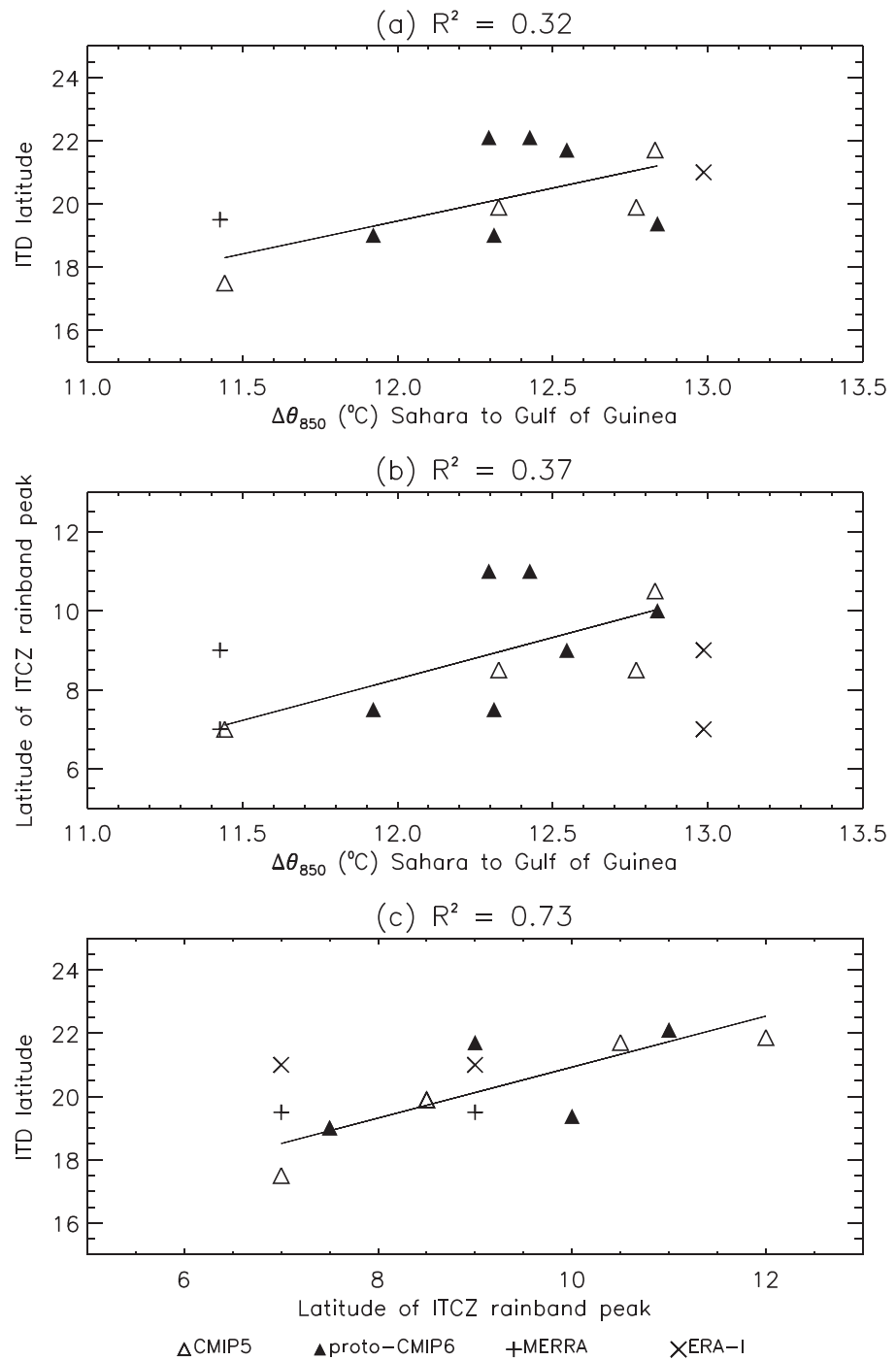


**Figure 4.** Scatter-plots showing the relationship between horizontal gradient in  $\theta_{850}$  between the Sahara and the Gulf of Guinea (defined as the difference between the box averages over the regions [10°W–10°E, 20–30°N] and [10°W–7°E, 5°S–3°N]) and: (a) the latitude of the ITD as determined from the location of the sign reversal of 10 m meridional winds averaged between 10°W and 10°E; (b) the location of the WAM rainband peak. (c) The relationship between the ITD and ITCZ rainband peak latitudes. Regressions are taken over the model values only as the reanalyses and satellite rainfall observations may not be consistent.

As discussed in the previous section, the notable effects on the WAM system of changes in the physical parameterizations between members of the same model family suggest more complex relationships between the WAM circulation, its rainfall distribution and the small-scale processes contributing to the overall energy and moisture budgets, consistently with the findings of Peyrillé *et al.* [2016]. In the next section, we investigate this further using the diabatic heating and moistening distributions from the models and reanalyses.

## 4. Diabatic Processes and Circulation Within the WAM

### 4.1. Documentation of the Meridional-Vertical Structures

Meridional cross sections shown in Figure 5 illustrate how the vertical structures of heating ( $Q_1$ ) and the effective heating due to drying ( $Q_2$ ), averaged over the two groups of models and from the two reanalyses, evolve from the Gulf of Guinea to the Sahara desert. The pressure velocity ( $\omega$ ) and meridional wind velocity are also shown in the figure.

ERA-Interim and MERRA reanalyses differ quite significantly in the details of the  $Q_1, Q_2$  cross sections, illustrating the strong influence of the underlying model physics in determining such variables. However, they both indicate a sloping transition of the diabatic components northward, as the cooling/moistening from the monsoon flow is raised above the warming/drying near the surface in the Sahel and Saharan regions. The maximum low-level drying occurs just south of the ITD (identified by the sign change (heavy black contour) of the meridional wind in Figure 5, right plots). The shallow and deep circulations highlighted by Hagos and Zhang [2010] and Peyrillé et al. [2016] are highlighted with the meridional wind and the pressure velocity: a shallow layer of heating and moistening associated with low-level clouds topped by subsidence over the ocean is replaced by deeper heating/drying and ascent associated with deep convection in the WAM rainband (7°N–12°N). At low levels, the southerly flow proceeds northward until it converges with the northerly flow from the Sahara at the ITD (Figure 5, right). The Sahel region (12°N–20°N) is more stratified as boundary layers deepen and the midtroposphere dryness favors rainfall evaporation. The shallow circulation also continues to transport moisture northward while intense ascent occurs in the 1000–600 hPa layer. Over the Sahara (20°N–30°N), the dry convective heating in deep boundary layers dominates. The models capture the main picture of these  $Q_1, Q_2$  distributions. They mainly differ in terms of strength and depth of the heating/drying in the rainband and in its latitudinal position (consistently with Figures 1a and 1b). Note that the second maximum of ascent at 20°N in MERRA and ERA-Interim is better represented in prototype-CMIP6 versions of GCMs.

The circulation in the meridional cross section, as balanced with  $Q_1$  ( $\overline{\psi_{diab}^{nd}}$ ), is shown with the zonal mean nondivergent stream function  $\overline{\psi^{nd}}$  in Figure 6 (see section 2.3 and Appendices A and B for details). Although somewhat circular in the sense that  $\overline{\psi_{diab}^{nd}}$  is expected to be in equilibrium with the circulation in the deep tropics, it gives information on the relative contribution of the heating to the zonal mean stream function. Consistent with Figure 5, their large-scale features agree quite well along the transect in the free troposphere, indicating that the large-scale nondivergent meridional circulation, i.e., the deep overturning cell in the ITCZ region (10°N) and the shallow ascent (20°N–25°N), mostly balances the diabatic heating distribution. The main departure between  $\overline{\psi_{diab}^{nd}}$  and  $\overline{\psi^{nd}}$  occurs on the southern flank of the SHL (over 15°N–25°N). The diabatic stream function places a further northward center of shallow circulation (minimum of  $\overline{\psi_{diab}^{nd}}$  located at 20°N, 800 hPa) compared to  $\overline{\psi^{nd}}$  which does not exhibit such a marked shallow circulation. This is consistent among reanalyses and models and shows that although turbulent heating is the main source of ascent over 15°N–30°N, it is counteracted by the effect of temperature gradients and transients such that the shallow ascent is placed further south. As expected, large meridional gradients of temperature prevail in the region making  $\overline{\psi_{diab}^{nd}}$  a less accurate diagnostic. It also means that the 3-D dynamics associated with horizontal gradients of pressure/temperature helps to locate the SMC further to the south.

### 4.2. Regional Analysis of Diabatic Heating and Drying

In the following subsections, we consider the heating and drying profiles averaged over four regions ranging from the Gulf of Guinea to the Sahara and sampling the meridional distribution of  $Q_1$  and  $Q_2$  (Figure 7 for CMIP5 and Figure 8 for prototype-CMIP6 configurations). This approach highlights the balance of the processes contributing to total heating/drying, and how they have evolved between different members of a given model family.

#### 4.2.1. Gulf of Guinea

The Gulf of Guinea region (5°S to 3°N) experiences low-level heating and net moistening associated with shallow convection and well-mixed stratocumulus-capped boundary layers (Figures 7a, 7b, 8a, and 8b). The midlevels and upper levels are dominated by longwave radiative cooling. The clouds and boundary layer structure in this region in summer play an important role in the formation of the monsoon temperature gradient, through evaporative cooling of the ocean surface and the formation of clouds that are capped at low levels by subtropical subsidence.

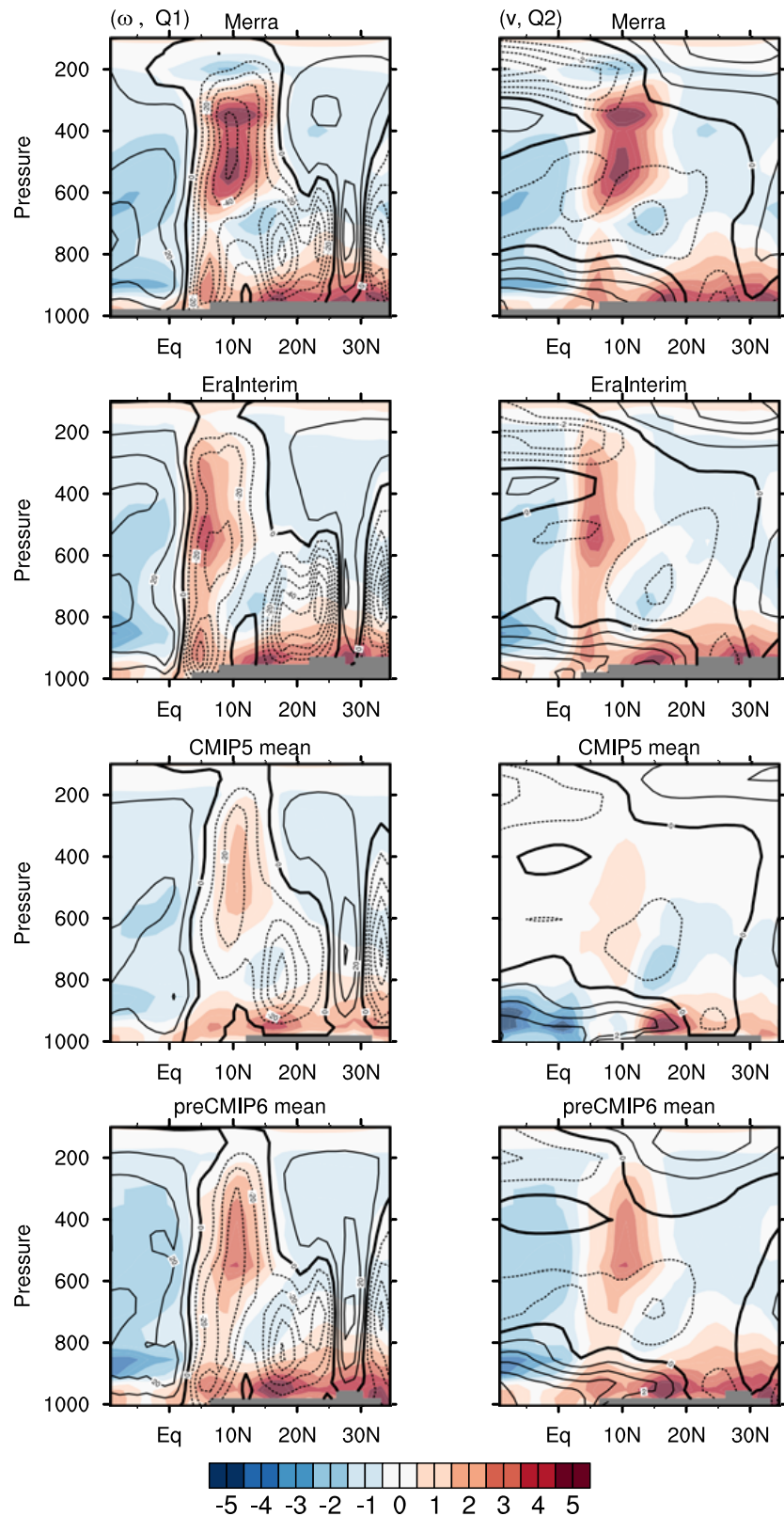


**Figure 5.** Latitudinal cross sections in JJA ( $10^{\circ}\text{W}$ – $10^{\circ}\text{E}$ ) of (left)  $Q_1$  (diabatic heating) in  $\text{K d}^{-1}$  (colored shading) and pressure velocity in  $\text{hPa d}^{-1}$  (contour every  $10 \text{ hPa d}^{-1}$ , negative values with dotted lines) and (right)  $Q_2$  (the effective heating due to drying from diabatic processes) in  $\text{K d}^{-1}$  (colored shading) and meridional wind in  $\text{m s}^{-1}$  (contour every  $0.5 \text{ m s}^{-1}$ , negative values with dotted line) for the African monsoon region, derived by the residual method from MERRA, ERA-I, and averages over the prototype-CMIP6 and CMIP5 model simulations.

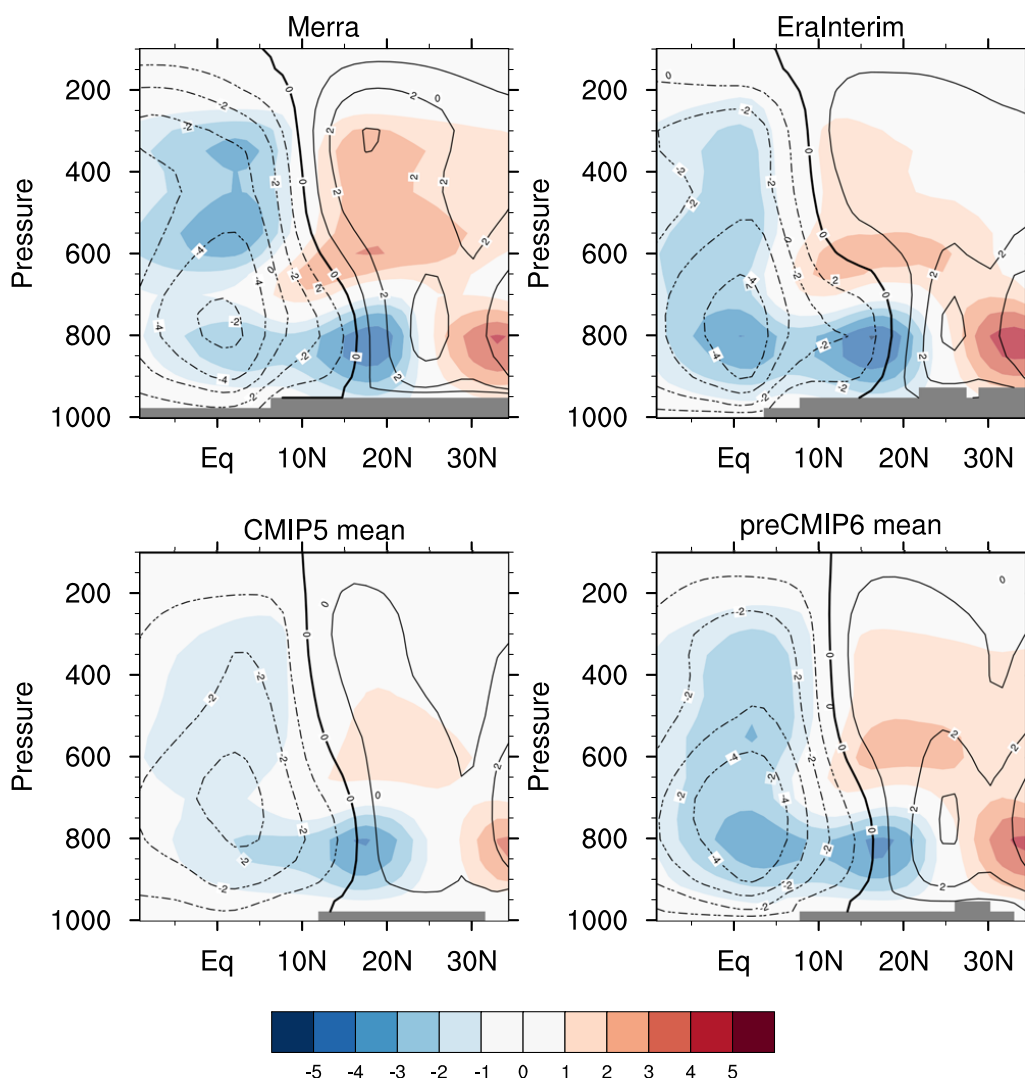


**Figure 6.** Meridional cross section of the ( $10^{\circ}\text{W}$ – $10^{\circ}\text{E}$ ) zonal mean mass stream function which balances  $Q_1$ , ( $\psi^{nd}$ , colors) and nondivergent mass stream function  $\psi^{nd}$  (contours at same intervals as color scale, negative contours dotted) for JJA, in the two reanalyses and averaged over the CMIP5 and prototype-CMIP6 model simulations. Units are  $10^{11} \text{ kg s}^{-1}$ .

The models and reanalyses demonstrate an overall consistent behavior in this region in terms of heating/cooling profiles. The details of the moistening structure exhibit a larger spread, in both the intensity and altitude of its peak at the top of the boundary layer. The lack of low-level clouds in CNRM-AM5 is associated with weaker radiative cooling above the boundary layer. In PreCNRM-AM6, more active shallow convection increases cloud cover and associated cooling/moistening. In comparison with HadGEM2-A, ProtoGA7 has a deeper mixed layer and increased cooling/moistening at the boundary layer top, consistent with a shift from cloud issued from the large-scale scheme to cloud produced by the shallow convection scheme (see supporting information, S1.2). Moistening in the lower levels is reduced in LMDZ5B due to the addition of drying from the cold pool parameterization (see supporting information Table S1 and section S1.3). In contrast, the NPv4.12bis and NPv4.12.OR11 configurations have reduced stratocumulus and increased boundary layer depth over the Gulf of Guinea compared with LMDZ5B, consistent with the activation of a thermal plume model in all regions in the new configurations, which was disabled in regions of strong inversion in LMDZ5B (see supporting information S1.3 and Hourdin *et al.* [2013b]).

The region of the Gulf of Guinea is thus mainly driven by low-cloud processes. Their overall effect in terms of heating/cooling is quite consistent across the models and reanalyses, the spread being driven by radiative processes. The spread in their moistening effect is large and probably has an impact on cloud cover and properties, and thus on the model spread in longwave radiative cooling.

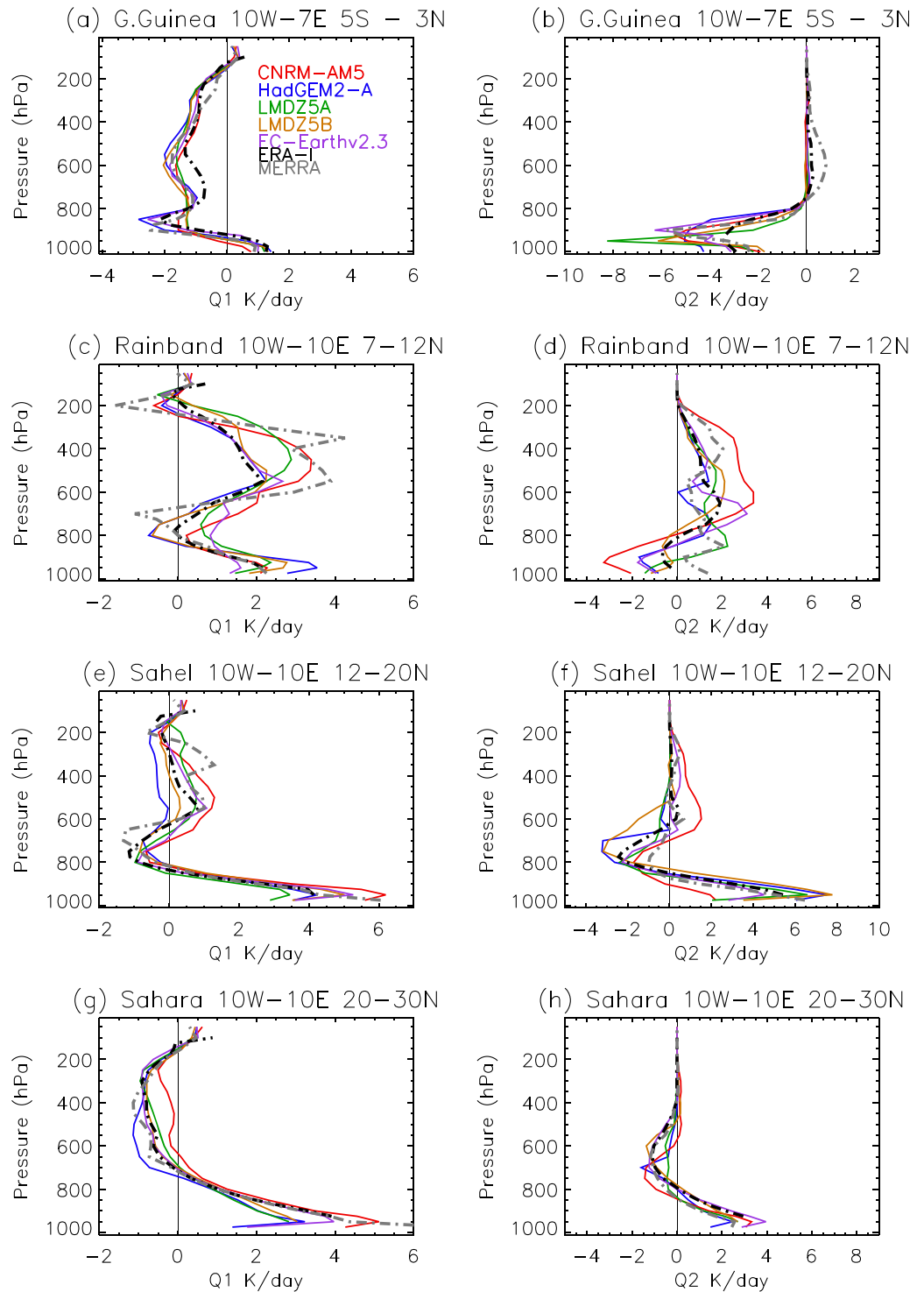


**Figure 7.** Total  $Q_1$  and  $Q_2$  profiles from the different physical parameterizations in the CMIP5 model configurations, averaged over subregions of the WAM region in JJA. Also shown are  $Q_1^{res}$  and  $Q_2^{res}$  derived from ERA-Interim reanalyses and  $Q_1$  and  $Q_2$  derived from MERRA reanalyses tendencies. Units:  $K\ d^{-1}$ .

#### 4.2.2. WAM Rainband

The overall magnitude and vertical structure of deep convective heating and drying in the main rainy region ( $7^{\circ}N$ – $12^{\circ}N$ ) is determined by the balance between boundary layer mixing, shallow and deep

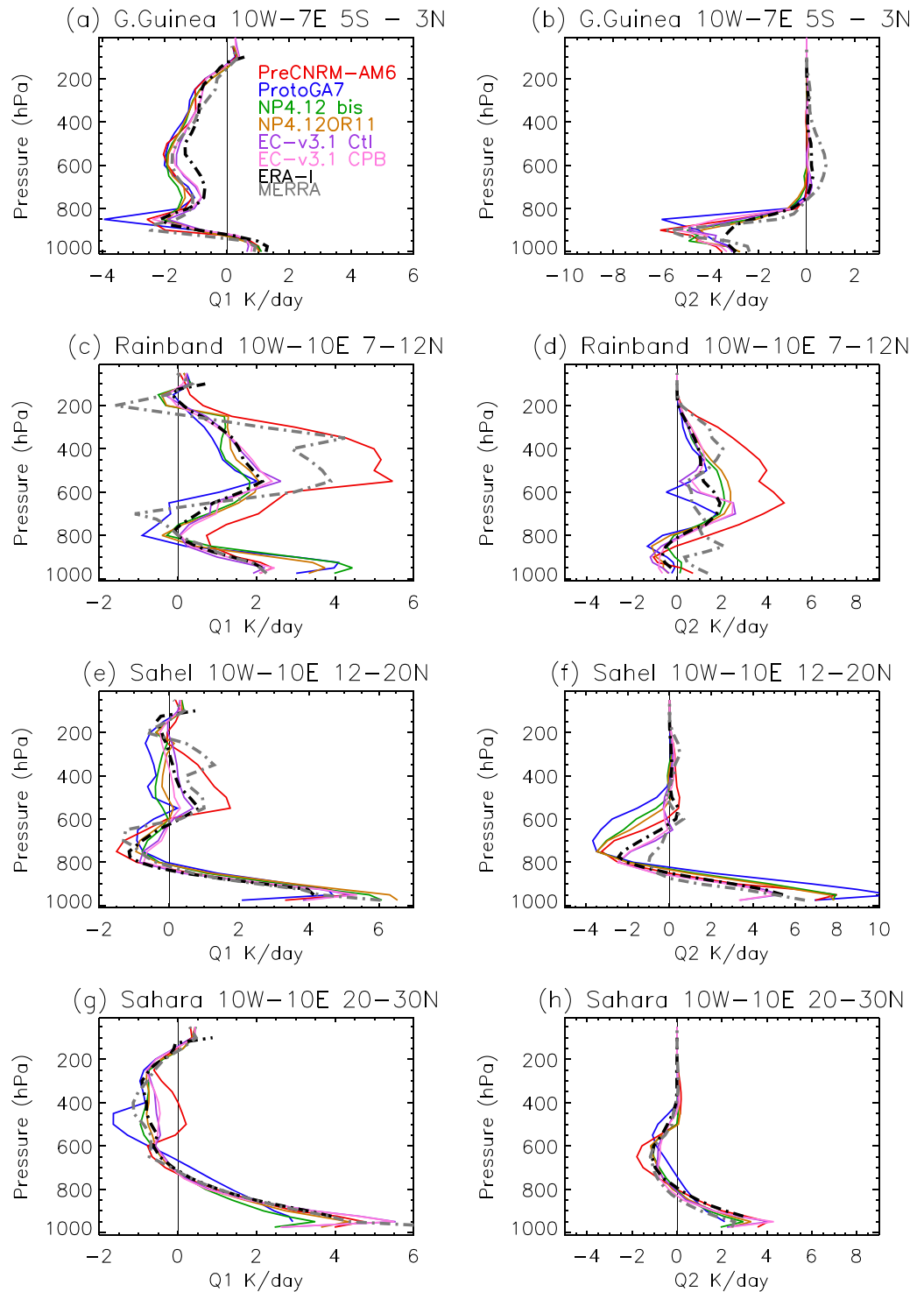
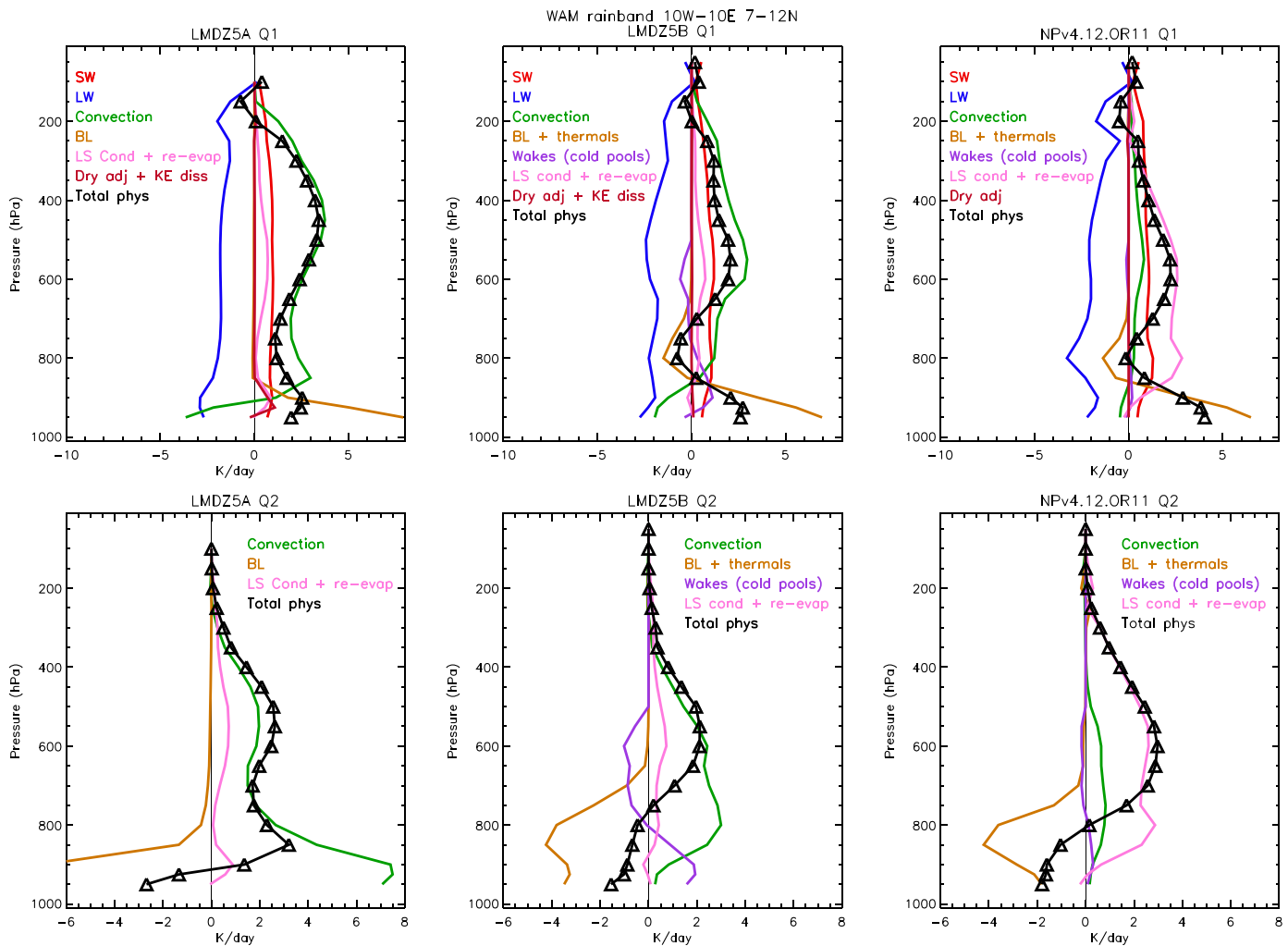


Figure 8. As Figure 7 but for the prototype CMIP6 configurations.

convection and large-scale cloud processes. As mentioned in section 4.1, the SMC is associated with low-level heating and moistening while the deep convection, large-scale cloud and precipitation processes combine to cool/moisten at the lower levels and heat/dry the free troposphere above. To first order, this structure is captured by the model simulations and reanalyses, but there is considerable spread, even between the two reanalysis data sets, particularly for  $Q_2$ .



**Figure 9.**  $Q_1$  and  $Q_2$  components from different diabatic heating sources in the WAM rainband region ( $10^{\circ}\text{W}$ – $10^{\circ}\text{E}$ ,  $7^{\circ}\text{N}$ – $12^{\circ}\text{N}$ ) from LMDZ5A, LMDZ5B and NPv4.12.OR11.

The spread in the intensity of the heating and drying peaks in the free troposphere is mainly driven by the amount of precipitation (compare Figures 7c, 7d and 8c, 8d with Figures 1a and 1b). The vertical structure of  $Q_1$  is rather consistent among models, even though it varies significantly both in the low levels, where it highlights different boundary layers, and in the midtroposphere and upper-troposphere, emphasizing different ability of convection to deepen. No consensus can be found for the profile of  $Q_2$ , underlying the requirements for better documenting and constraining its properties.

The passage from LMDZ5A to LMDZ5B and NPv4.12 highlights the impact of adding a shallow convection scheme (see supporting information Tables S1 and S2), which produces deeper boundary layers with more mixing and allows some cooling just above (Figure 9). The latter even dominates heating by deep convection. In the midtroposphere and more particularly the upper-troposphere, the modification of the mixing formulation between deep convection and its environment, which makes convection more sensitive to environmental dryness, yields a decrease of deep convective heating from LMDZ5A to LMDZ5B (also true over the Sahel). In the NPv4.12 configurations (Figure 9, right), the stochastic triggering modifies the balance between shallow and deep convection, leading to less frequent activation of deep convection. As a result, the large-scale condensation/precipitation takes over, strongly impacting the ratio between large-scale and convective precipitation (see supporting information Table S2 and section S1.3).

In PreCNRM-AM6, the balance between large-scale condensation and convection is also radically modified compared to CNRM-AM5, but also to most of the other models (Figure 10). While the convective scheme is

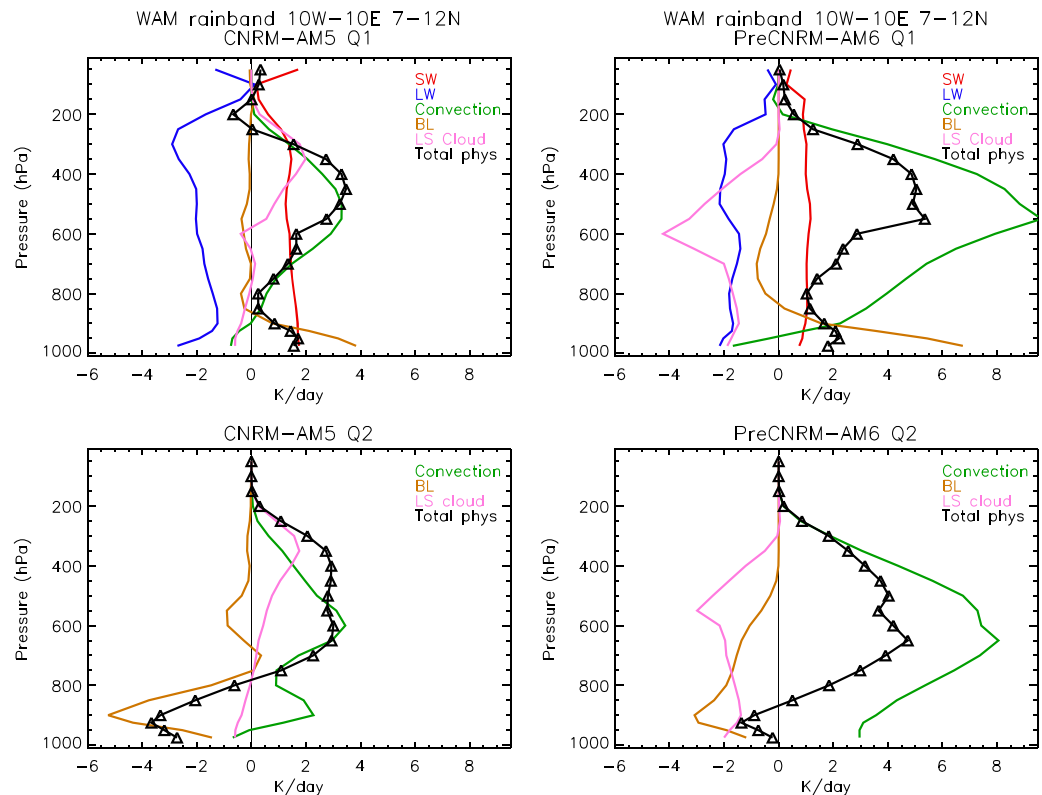


**Figure 10.**  $Q_1$  and  $Q_2$  components from different diabatic heating sources in the WAM rainband region ( $10^{\circ}\text{W}$ – $10^{\circ}\text{E}$ ,  $7^{\circ}\text{N}$ – $12^{\circ}\text{N}$ ) from CNRM-AM5 and PreCNRM-AM6.

very active, producing considerable rain and cloud water, it detrains in the dry environment a large part of it, which is then largely evaporated before reaching the ground (see the large-scale cloud contribution in Figure 10). It remains unclear how this balance between convective and large-scale latent heating, with different shape and timescale, might impact the WAM circulation. Similar changes are also seen between ProtoGA7 and HadGEM2-A (not shown) although in this case, the total heating is slightly reduced as the changes in the cloud and microphysics schemes add more cooling at mid-levels and less heating at upper levels.

Overall, the spread across models in this region is related mostly to differences in the representation of convection, clouds, and precipitation, including the relative balance between shallow and deep convection. This is explored further in section 4.3.

#### 4.2.3. Sahel Region

Moving northward ( $12^{\circ}\text{N}$  to  $20^{\circ}\text{N}$ ), the deep precipitating convection is gradually replaced by dry convective mixing. At low levels, there is heating/drying associated with turbulent eddies, topped by a cooling/moistening layer associated with convective downdrafts. In the free troposphere, there are contributions from both radiative cooling and convective/stratiform heating, with the overall average profile depending, in part, on the location of the main rainband relative to our chosen averaging region.

The Sahel profiles in Figures 7e, 7f and 8e, 8f show some spread in this complex structure, particularly in the amount of low-level heating/drying and in the vertical extent of moistening above this. The low-level drying and midlevel moistening are largest in ProtoGA7, which, among many other changes, includes a representation of forced shallow cumulus clouds within boundary layer capping inversions (see supporting information S1.2). This increases the occurrence of shallow convection in the Sahel region. Similarly, in LMDZ5B, the inclusion of a thermal plume model and a cold pool parameterization, along with modifications to the deep convective triggering and closure, were shown in case studies to improve the diurnal cycle of both shallow and deep convection over the Sahel region [Couvreur *et al.*, 2015] (see supporting information S1.3). This configuration also shows increased heating/drying at low levels and cooling/moistening above (Figures 7e and 7f). The NPv4.12 configurations from LMD show further increases in low-level heating/drying as the

rainband is shifted south out of the averaging region. The change to the ORCHIDEE11 scheme in NPv4.12.OR11 is associated with an additional increase in the near-surface heating and drying.

In CNRM-AM5, where the rainband is further north than in the other model simulations, the contribution from deep convection to the regionally averaged profile is larger (Figures 7e and 7f). Although the rainband is shifted southward in PreCNRM-AM6, the changes to the convection and large-scale cloud schemes (see section 4.2.2 and supplementary information S1.1) are associated with increased heating in the free troposphere and increased moistening at midlevels. In contrast, a southward shift in the rainband in EC-Earthv3.1 Ctrl and CPB reduces the contribution from deep convection to the free tropospheric heating.

Overall, in a similar manner to the rainband region, the spread across models in this region is related mostly to differences in the representation of convection, clouds and precipitation, including the relative balance between shallow and deep convection. In addition, the representation of surface exchange and dry convective mixing start to become important in this transition region.

#### 4.2.4. Saharan Region

The Saharan region (20°N to 30°N) is dominated by dry convective mixing, with heating/drying at low levels and cooling/moistening above, plus longwave radiative cooling and shortwave heating throughout the troposphere. This overall structure is demonstrated by the model simulations and reanalyses (Figures 7g, 7h and 8g, 8h), although there is some variation in the near-surface heating and drying, as well as in the vertical extent of the dry convective mixing and the balance of SW and LW heating/cooling.

The heating and drying extends to greater depth in ProtoGA7 compared with HadGEM2-A. The cooling at around 500 hPa in Figures 7g and 8g indicates the presence of cloud in this region which extends slightly deeper in ProtoGA7 than in HadGEM2-A. The individual heating increments (not shown) suggest more absorption and reradiation by aerosols there, with increases in both SW heating and LW cooling; the latter adds to the extra longwave cooling from cloud to produce an overall increase in cooling.

Similarly, in PreCNRM-AM6 the heating and drying extends to a slightly greater depth than in CNRM-AM5 and the excessive total heating at lower levels in CNRM-AM5 is reduced. Examination of the individual heating components shows that shortwave heating is reduced in the midlower troposphere below about 500 hPa and longwave cooling decreases in line with this (Figure 11). This is related both to an increased surface albedo over the Sahara and to changes in the aerosol (particularly dust) optical properties in this configuration, whereby shortwave absorption by dust is reduced while longwave absorption by dust is slightly increased. Boundary layer heating increases and there is also a notable contribution from large-scale cloud and convection in this region in PreCNRM-AM6 which was not present in CNRM-AM5 and which is associated with the additional cooling/moistening at around 650 hPa.

In LMDZ5B and NPv4.12 configurations, the inclusion of the thermal plume model is associated with deeper dry convective mixing than in LMDZ5A, while the change to the ORCHIDEE11 scheme in NPv4.12.OR11 increases the near-surface heating and drying (Figures 7g and 7h).

Overall, the spread across models in this region is related mostly to differences in the representation of aerosols and clouds (affecting the radiative heating), surface exchange and boundary layer mixing in the dry convective layer.

#### 4.3. Using Bulk Budgets of Temperature, Humidity, and MSE to Synthesize Model Behavior

The analysis in the previous subsections illustrates that, while the models represent well the overall distribution of  $Q_1$  and  $Q_2$  in the WAM region, they may result from a very different balances of processes depending on the specific model. Here we attempt to synthesize the results to shed light on these different balances by comparing vertically integrated heating ( $\langle Q_1 \rangle$ ) and drying ( $\langle Q_2 \rangle$ ) from the different diabatic sources (Figures 12 and 13) as well as the diabatic tendencies of column-integrated MSE given by  $\langle Q_1 - Q_2 \rangle$  (Figure 14). See Appendix C for details of the calculation of these integrals. It should be noted that different model configurations may not partition the heating/drying from part of the physics in exactly the same way, so that direct comparison between the models is not possible. Nevertheless, this analysis provides some insight into how the individual model configurations achieve their total heating and drying in each region, which can be further investigated in future individual model studies.

We see that, over the Gulf of Guinea, radiative cooling is a prevailing component of  $\langle Q_1 \rangle$ , partly offset by boundary layer and convective heating in all models and either cooling/heating, from large-scale cloud

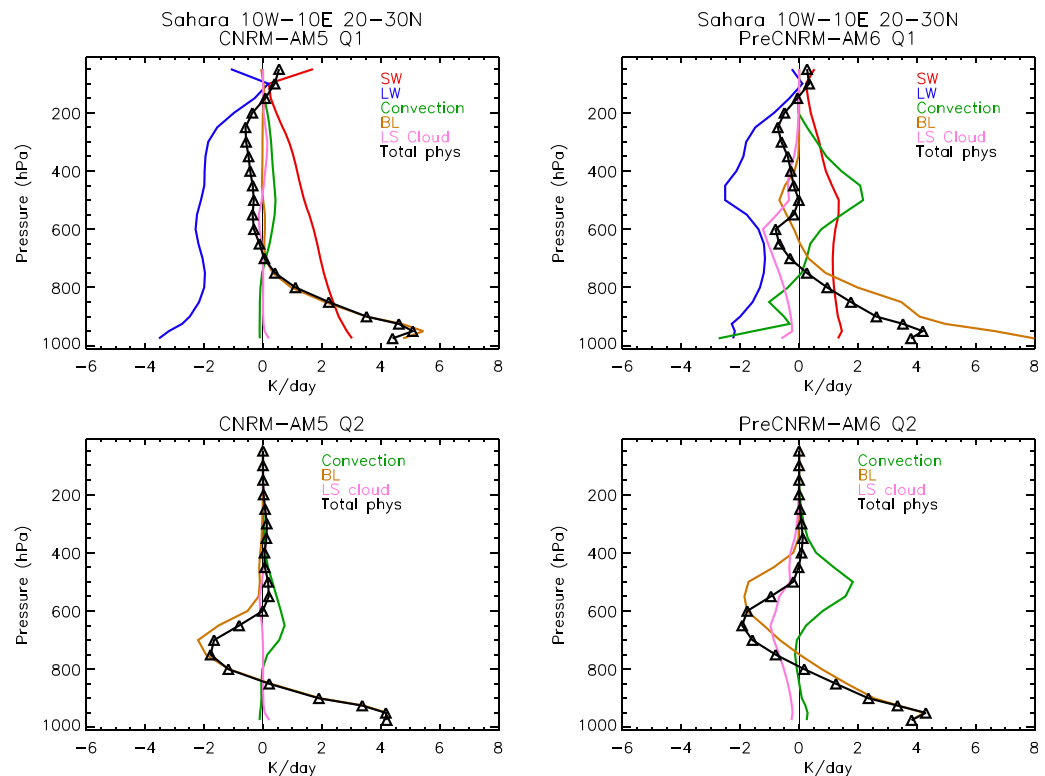


**Figure 11.**  $Q_1$  and  $Q_2$  components from different diabatic heating sources in the Saharan region ( $10^{\circ}\text{W}$ – $10^{\circ}\text{E}$ ,  $20^{\circ}\text{N}$ – $30^{\circ}\text{N}$ ) from CNRM-AM5 and PreCNRM-AM6.

depending on the model assumptions (Figure 12).  $\langle Q_2 \rangle$  in this region is dominated by moistening from boundary layer mixing, which shows the region is a moisture source for the WAM. A striking feature is the relative consistency among models on the sign, intensity and leading contribution of  $\langle Q_1 \rangle$  and  $\langle Q_2 \rangle$ , showing that from an energetic point of view, the GCMs perform well in the Gulf of Guinea. As mentioned in the previous section, it is more difficult to converge toward a common vertical profile of heating/drying due to the representation of stratocumulus clouds. From a moist static energy perspective (Figure 14),  $\langle Q_1 - Q_2 \rangle$  (MSE) shows a sink of energy of  $\sim 50 \text{ W m}^{-2}$  by radiative cooling quasi-balanced by surface evaporation. It is noticeable that there is a good agreement among models on the intensity of the surface latent heat fluxes while radiative cooling shows a larger spread.

In the WAM rainband, net radiative cooling is balanced by deep convection and to a lesser extent by PBL heating. Depending on model parameterization philosophy, large-scale condensation or evaporation occurs, contributing to or balancing the convective heating (Figure 12). The leading contribution to  $\langle Q_2 \rangle$  is the convective drying balanced by surface evaporation. Although specific contributions from convection, turbulence, and radiation vary among models, the overall balance is a net heating/drying, showing the key contribution of deep convection.  $\langle Q_1 - Q_2 \rangle$  shows the same kind of equilibrium as over the Gulf of Guinea except the result is a net gain of column MSE largely due to the moistening by surface latent heat fluxes.

The Sahel region shows a transition toward a drier regime in which the balance is the same as for the WAM with the exception that surface sensible heat fluxes now have a greater contribution. This is exemplified in Figure 14 with a large contribution from sensible heating that compensates radiative cooling. All models still agree on the sign of  $\langle Q_1 - Q_2 \rangle$  which shows an increase of column MSE in the region but with a large spread.

The Sahara shows a balance between radiative cooling and surface heating. Note that these two terms are large and the net  $\langle Q_1 \rangle$  mainly results from their difference, thus showing no common agreement among models. Although the SHL is dominated by dry processes, presumably easier to represent, it is the region where the GCM shows the higher spread and disagreement even on the sign of  $\langle Q_1 \rangle$ . This may have implications for the representation of the monsoon circulation since the meridional gradient of energy is a key

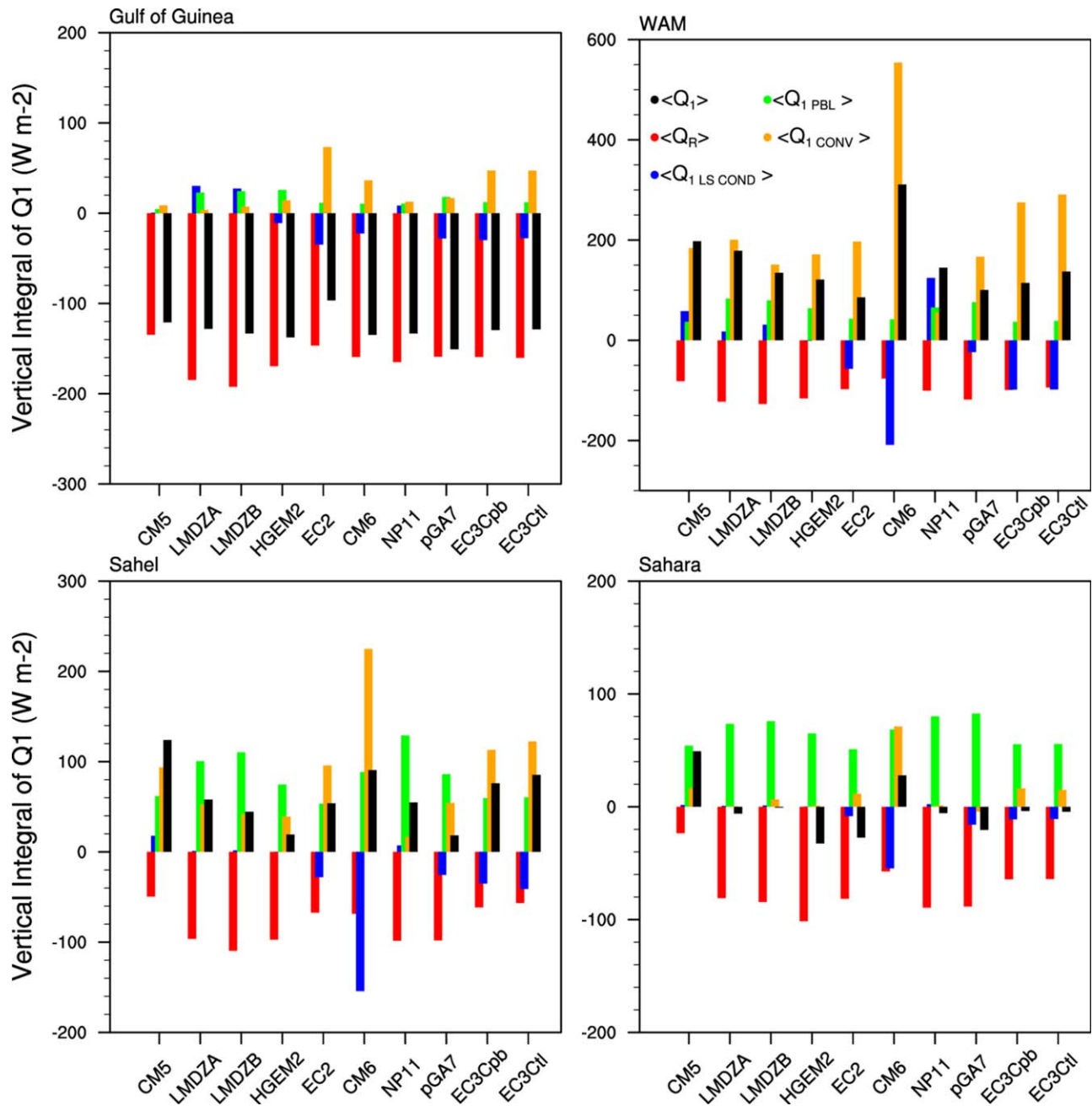


**Figure 12.** Vertically integrated  $Q_1$  and the contributions from different physical processes, for the four key areas ( $W m^{-2}$ ). Contributions from: radiation (red), large-scale condensation (blue), convection (orange), boundary layer mixing (green). Note the variation in scale of the vertical axes. Note also that partitioning by each model configuration within these broad definitions may not be exactly the same; therefore, these results are for overview purposes only.

driver of meridional overturning.  $\langle Q_1 - Q_2 \rangle$  shows that humidity is a weak contributor to the column MSE, although the sign of surface evaporation varies with the model.

### 5. Linking the Basic Features of the WAM to Diabatic Heating

The analysis in section 3.3 showed how the meridional temperature gradient between the Saharan and Gulf of Guinea region is moderately related to the ITD and ITCZ latitudes, which themselves are strongly correlated. Here we investigate the relationship between the diabatic heating and the WAM circulation by correlating various regionally averaged quantities with the zonal mean ( $10^\circ W$  to  $10^\circ E$ ) cross sections of

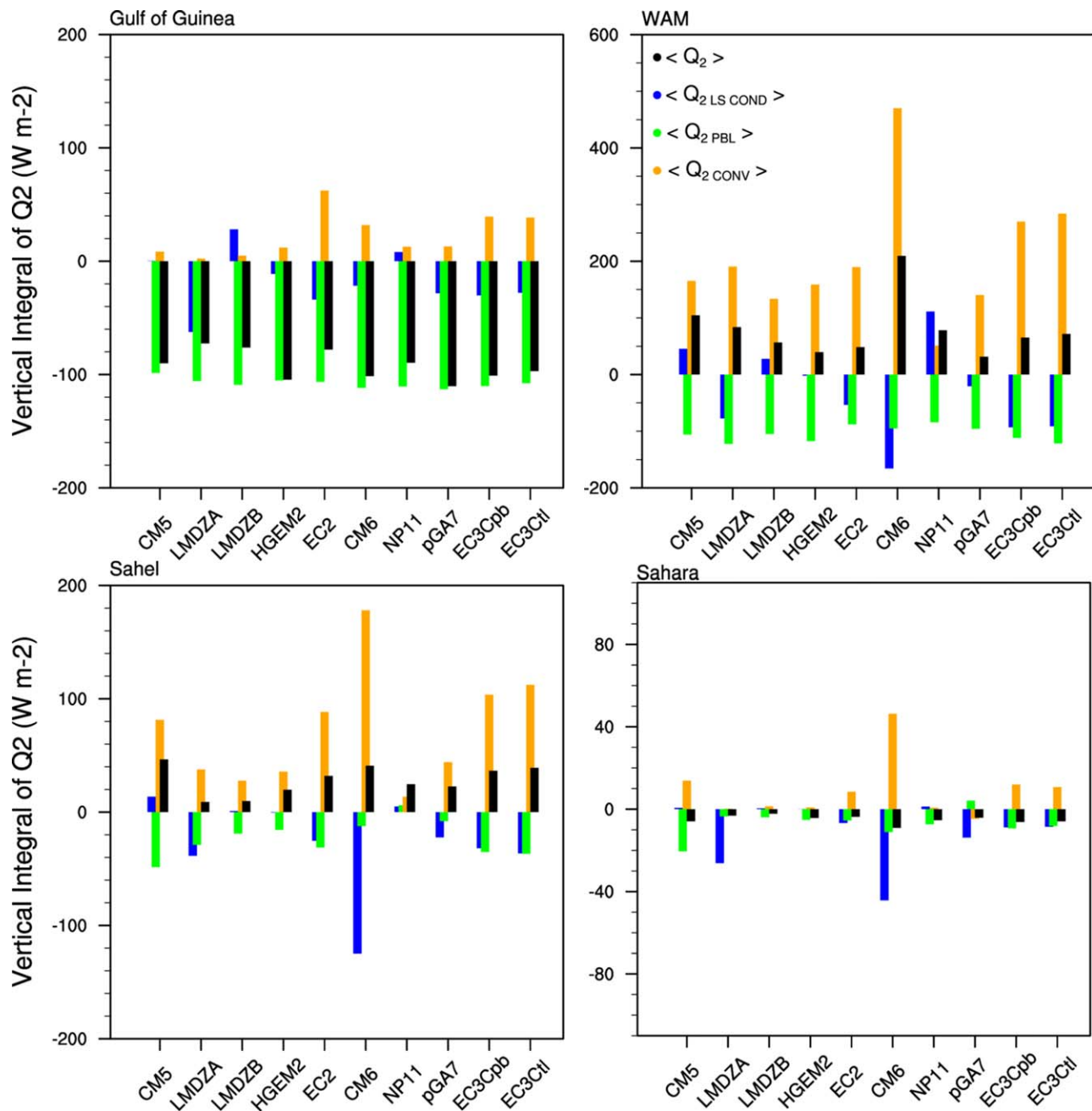


**Figure 13.** Vertically integrated  $Q_2$  and the contributions from different physical processes, for the four key areas ( $W m^{-2}$ ). Contributions from: large-scale condensation (blue), convection (orange), boundary layer mixing (green). Note the variation in scale of the vertical axes. Note also that partitioning by each model configuration within these broad definitions may not be exactly the same; therefore, these results are for overview purposes only.

total heating  $Q_1$  and its radiative component  $Q_R$  from the ensemble of model simulations and reanalyses (Figure 15). This quantifies how much the intensity of a specific feature of the WAM is correlated with the diabatic heating at some (latitude, altitude) in the meridional WAM transect. Regions with high correlation thus underline a significant link between  $Q_1$  and/or  $Q_R$  and the considered WAM feature, assuming the set of different models provides different realizations of the WAM. The same analysis performed for the diabatic drying  $Q_2$  is not shown, as it provides very similar results to  $Q_1$ .

The ITCZ ascent intensity (negative pressure velocity) is highly correlated with the diabatic heating (and drying, not shown) within the ITCZ (Figure 15a, correlation coefficient  $>0.7$ ) above 800 hPa, as expected since the

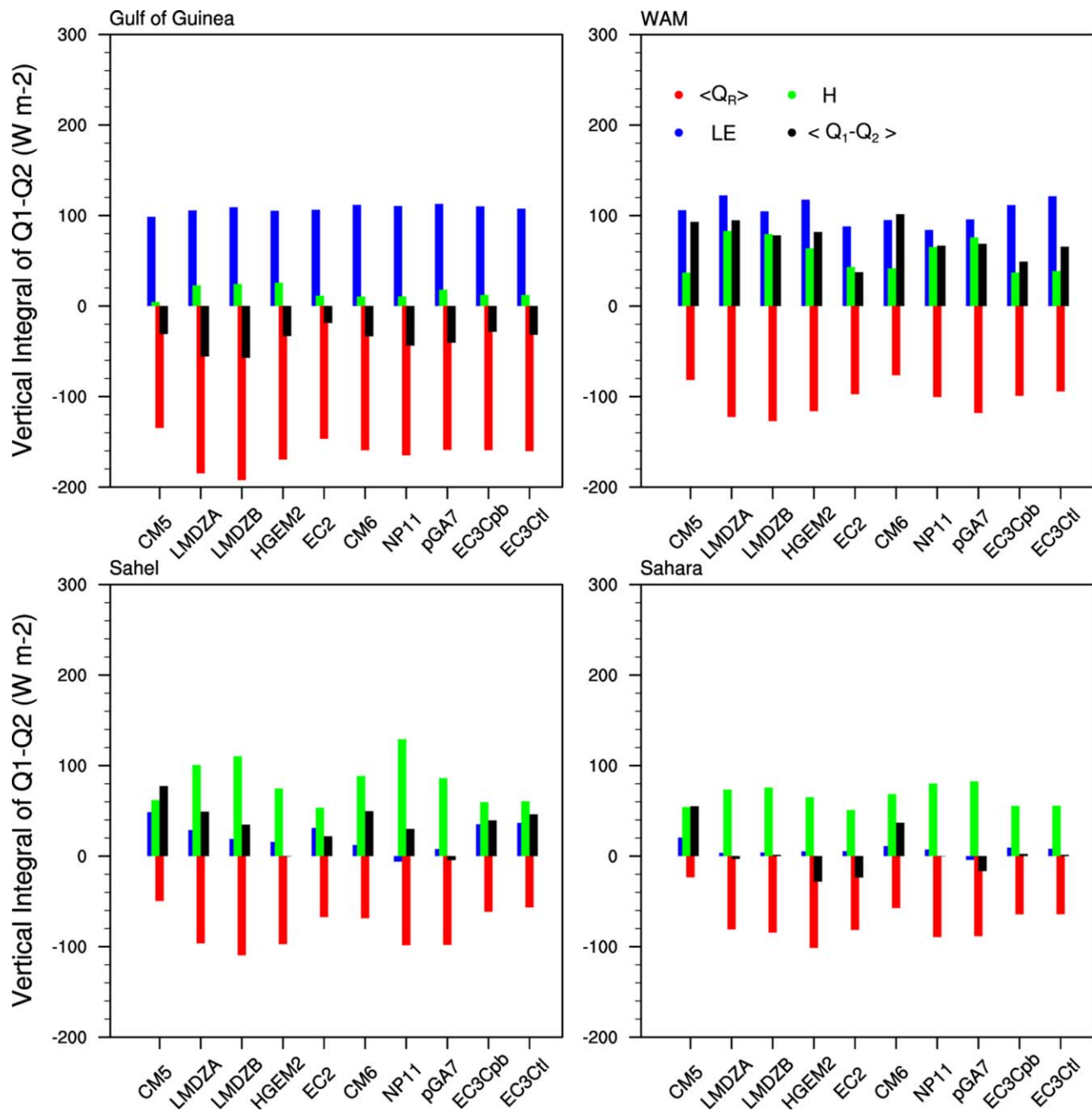


**Figure 14.** Vertically integrated  $Q_1$  minus  $Q_2$  (black) and the contributions from different physical processes, for the four key areas ( $W m^{-2}$ ). Contributions from: radiation (red), surface latent heat fluxes (blue), sensible heat fluxes (green). Note that partitioning by each model configuration within these broad definitions may not be exactly the same; therefore, these results are for overview purposes only.

vertical advection mostly balances the heating in the deep convective area. More surprising is the large area of high correlation at upper level (above 600 hPa) over Sahara and North Sahel. Intuitively a stronger cooling over the SHL could be associated to a more intense subsidence and by continuity to a stronger ITCZ ascent. The resulting correlations suggest the opposite behavior: a weaker cooling (higher  $Q_1$ ) over the Sahara is linked to an increased ITCZ ascent (negative pressure velocity). As a significant high correlation with  $Q_R$  (Figure 15b) is found on the edges and at the top of the large area of high correlation with  $Q_1$  (Figure 15a), it may reflect that a stronger ITCZ induces a larger region of convective activity associated with clouds at midlevels and upper levels which reduces the atmospheric cooling. A too strong (weak) ascent in the ITCZ is thus linked to a too weak (intense) cooling over the SHL free troposphere.  $Q_R$  might be a leading process to explore in GCMs.

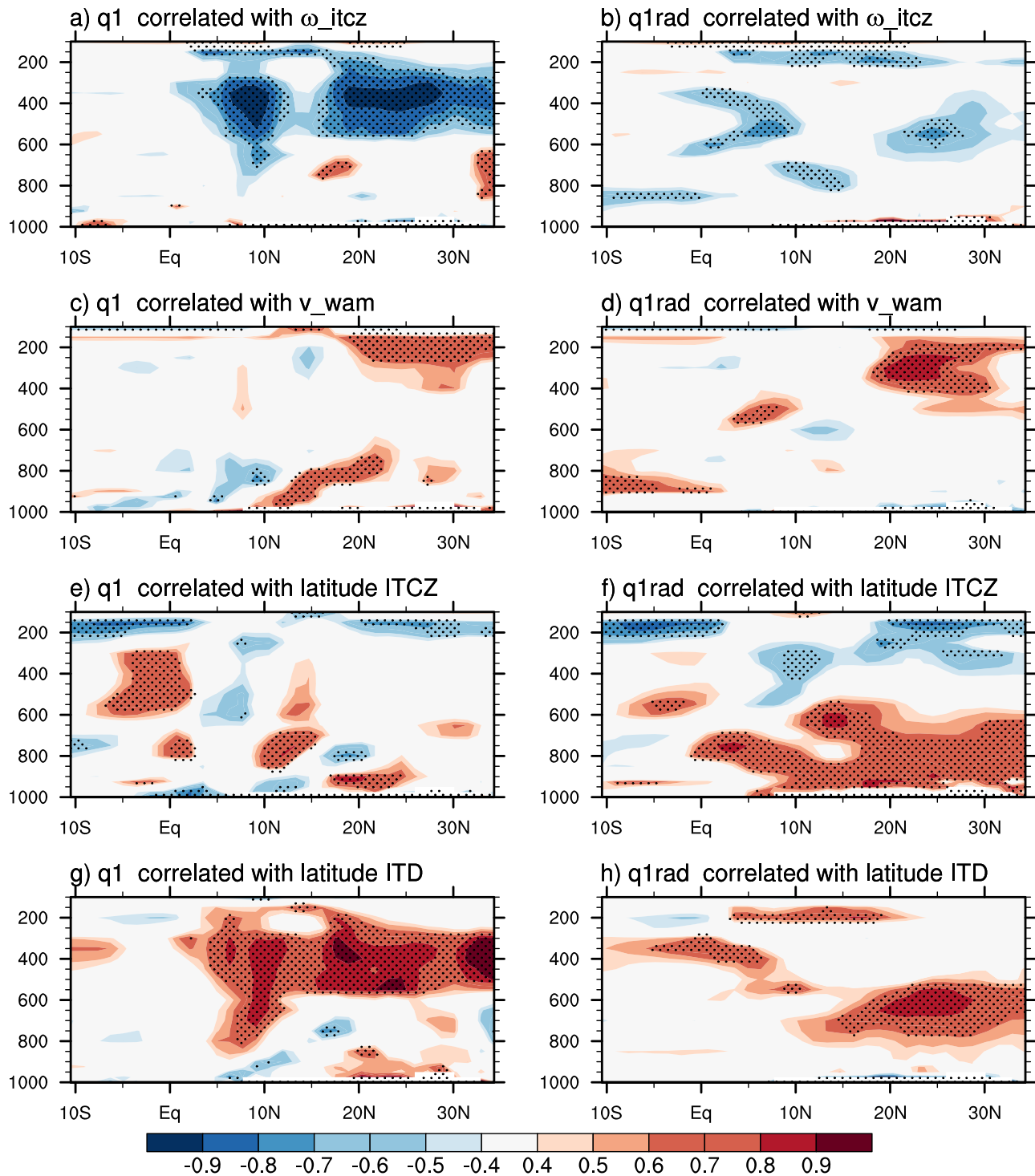


**Figure 15.** Meridional cross section of intermodel correlation between  $Q_1$  (left),  $Q_R$  (right) and (a and b) the average pressure velocity within the WAM region ( $7^{\circ}\text{N}$ – $12^{\circ}\text{N}$ , 600–300 hPa), (c and d) the averaged monsoon meridional wind within the WAM region ( $7^{\circ}\text{N}$ – $12^{\circ}\text{N}$ , 925–850 hPa), (e and f) the rainband peak latitude, and (g and h) the ITD latitude. Areas of significant correlation at 0.95 using a Student’s  $t$  test are dotted.

The intensity of the monsoon flow (defined as the average of the meridional wind over  $7^{\circ}\text{N}$ – $12^{\circ}\text{N}$ , 925–850 hPa) is correlated with the low-level heating over the Sahel, around  $10^{\circ}\text{N}$ – $20^{\circ}\text{N}$ , following the northward deepening of the boundary layer (Figure 15c). This most likely reflects the interaction between the monsoon flow and the boundary layer mixing. The monsoon flow intensity also correlates with the  $Q_1$  above the

Sahara at upper levels (above 400 hPa) partly due to less cooling as suggested by  $Q_R$  (Figure 15d). A key result here is that the stronger the ITCZ ascent and the stronger the large-scale monsoon circulation, the weaker the radiative cooling over the Sahara.

The latitudinal location of the ITCZ is correlated with heating (and drying, not shown) at midlevels over the Gulf of Guinea (5°S to 3°N; Figure 15e) and (perhaps inevitably) with the amount of heating/drying on the northern side of the rainband itself. In particular, the rainband is further north when the radiative cooling over the ocean in the free troposphere is weaker. On the northern side of the ITCZ (20°N), there is a dipole of significant correlations in the low levels that might be the signature of the PBL tendencies. In good agreement with previous results [Peyrillé *et al.*, 2016; Thorncroft *et al.*, 2011], a more intense PBL mixing, standing for a more intense SHL, is associated with a further north ITCZ location. The correlation structure with  $Q_R$  (Figure 15d) exhibits a large area of positive correlation over the continent, deepening from the coast (5°N) to Sahara up to 600 hPa corresponding to SHL depth. A stronger radiative heating over the Sahel and Sahara favors the northward penetration of the ITCZ. Near the tropopause the negative correlation is seen to be partly due to the radiative component.

The ITD latitude correlates (Figure 15g) with the diabatic heating (and drying, not shown) throughout the troposphere over the rainband region, and above 600 hPa over the Sahel and the Sahara. This correlation pattern resembles the one for the ITCZ ascent intensity (Figure 15a), suggesting that a stronger ITCZ is associated to a further north SMC. On the contrary, the correlation pattern with  $Q_R$  is quite different with a large positive area in the upper part of the heat low, suggesting that the ITD shifts northward when the radiative cooling is weaker. The chain of processes is complex and different explanations can be given, such as the role of aerosols and clouds at the top of this deep boundary layer [Roehrig *et al.*, 2013]. Further studies are needed, but the large changes noted from CNRM-AM5 to PreCNRM-AM6 are consistent with the above analysis. Indeed, major changes relative to albedo and aerosols properties have been made for the CNRM model, resulting in a decrease of  $Q_R$  in the SHL (Figures 11a and 11b) which is associated with a southward shift of both ITD and ITCZ in the prototype-CMIP6 version. In the rainband region (7°N–12°N), the positive correlation within the 800–600 hPa layer shows that the heating from cloud and precipitation processes are linked to a further north position of the ITD. There, again, the chain of processes is complex and will deserve more investigation.

The present diagnostic multimodel analysis emphasizes the complexity of the WAM system. The local and remote influence of the diabatic heating along a meridional transect going from 10°S to 40°N on the properties of the WAM has been documented here at the monthly scale, providing some interesting hypotheses to be tested in a numerical framework. In particular, the relationship between heating over the Saharan free troposphere and the WAM features appears an original result and deserves more investigation.

## 6. Discussion

As indicated by several past studies [e.g., Roehrig *et al.*, 2013; Hourdin *et al.*, 2010; Xue *et al.*, 2010], the representation of the climatological features of the WAM in a climate model is not straightforward. As an emergent phenomenon, the simulation of a monsoon system requires the correct representation of the many physical processes involved (radiative heating, turbulent mixing, convective transport of heat, moisture and momentum, microphysical phase changes and associated latent heating, dynamical transports, and frictional effects), all occurring on a range of times and space scales, in order that the correct mean features emerge. Variations in the representation of such processes between models, even between members of the same model family, make drawing clear conclusions about the role of the different physical parameterizations and dynamical cores on simulation of the mean monsoon extremely difficult.

However, the results of our study do highlight various interesting aspects which may warrant further study. We find that weaker net cooling in the Saharan region (which is related to aerosol properties, surface albedo, and the amount of cloud) promotes larger ascent in the ITCZ, a more intense monsoon flow and an ITD that is further north. However, despite a strong relationship between the ITCZ and ITD latitudes, the areas where they correlate with  $Q_1$  are different. It appears that the ITCZ position is related to radiative cooling over the Gulf of Guinea, with more cooling promoting a more southward ITCZ position. The ITD location is also strongly related to heating and drying in the WAM ITCZ region, while the intensity of the SMC is also related to the boundary layer mixing and shallow convection over the Sahel.

It should be noted that these relationships are only analyzed at the monthly time scale, and thus might be nuanced when considering the submonthly time scale. However, our analysis of the contributions to the  $Q_1$  and  $Q_2$  distributions from different physical processes, in models which represent these processes in different ways, improves our understanding of the WAM system and leads us to the following general conclusions which may be helpful for future model development:

1. The move toward integrated cloud and convection schemes (such as in PreCNRM-AM6 and ProtoGA7) alters the balance of large-scale and convective clouds and rainfall and is associated with large-scale shifts in the rainband.
2. Shallow convection plays an important role in cooling and moistening the lower levels in the WAM region (improved by the thermal plume model and bi-Gaussian cloud scheme in LMDZ5B as well as the PCMT scheme in PreCNRM-AM6).
3. Radiative forcing over the Sahara, which is related to the concentration and type of aerosols, the representation of clouds, and surface albedo, influences the northward progression of the rainband (improved in both PreCNRM-AM6 and ProtoGA7) and the ITD.
4. Improving the representation of the boundary layer and stratocumulus clouds over the Gulf of Guinea (e.g., in the MetUM, CNRM, and LMD families through various changes to the boundary layer and convection schemes) contributes to better representation of the temperature and moisture gradients associated with the monsoon flow.

As noted in section 4.1, it is hard to draw causal relationships between changes in  $Q_1$  and changes in the circulation. Part of the problem lies in interaction between the two, which cannot be addressed using a diagnostic methodology and climatological fields, because interactions and feedbacks are taking place at shorter timescales. A paper by *Chadwick et al.* [2017] applies different aspects of the diabatic heating distributions, from the different models and in the four key regions identified above, to an idealized dry dynamical core, in order to shed light on their influence on the monsoon circulation. The question of how the GCM circulation biases can be decomposed by processes contributing to  $Q_1$  is being addressed using a two-dimensional dry simple model and will be reported on in a future paper.

As noted at the start of this paper, none of these newer configurations represents a final model setup and further work will be required at each modeling center before the configurations are officially released. Further work will be needed at the individual modeling centers, using detailed comparisons and possibly further sensitivity tests between members of the same model family, in order to draw firmer conclusions from these experiments which could then be applied in other model configurations.

## 7. Conclusions

We have analyzed the diabatic heating distributions and the WAM characteristics in atmosphere-only simulations from four model families whose original configurations were used in CMIP5. Significant model development has been carried out within each model family in preparation for CMIP6. Although these prototype configurations are far from finalized, they provide both a range of realizations of the WAM system and insight into the contributions to the diabatic components from different physical processes. This has allowed us to analyze relationships between the physical processes and the WAM circulation which both improve our understanding of the WAM and have potential implications for influencing the direction of future model development.

We find that the northward extent of the WAM rainband is related to the vertical structure of both heating and moistening processes in the monsoon rainband as well as the meridional gradients related to the strength of the SHL and the subtropical high pressure region over the Gulf of Guinea. Radiative heating and cooling, convection, cloud and precipitation processes, and boundary layer mixing play important, but differing, roles in different parts of the meridional transect. Improvements to the representation of aerosols, additions to boundary layer and shallow convection schemes such as a thermal plume model, the representation of cold pools and forced shallow cumulus clouds, and the move toward integrated cloud and convection schemes, all contribute to the representation of this complex system in current GCMs. It is notable that the results from some of the prototype-CMIP6 configurations (in particular, PreCNRM-AM6) differ as much from their CMIP5 "parents" as they do from one another. This illustrates the substantial impact of new physical parameterization development on the simulation of important phenomena such as the WAM.

Although we have so far only analyzed the monthly climatologies of these diabatic components, time-varying monthly data are also available which could shed light on interannual variability and teleconnections. In addition, increments to the horizontal winds from the relevant parameterizations were also saved from the model runs. These represent the apparent momentum source,  $Q_3$ , defined in *Redelsperger and Lafore* [1994]. Future work could also include analysis of submonthly diabatic heating variations in order to investigate their role in the WAM onset and in intraseasonal variability such as African easterly waves and their coupling with convective rainfall, following the work of *Poan et al.* [2014].

For the first time, the diabatic heating components from different models, and their horizontal and vertical distribution in the WAM region, are presented and compared, with the added benefit of being able to make comparisons between different members of the same model family, allowing some traceability between configurations. Although further, more detailed, comparisons are required, this unique data set will provide model developers with insight into the complex relationship between diabatic processes and circulation in this key tropical region.

### Appendix A: Diagnostic of a Diabatic Stream Function

Starting from the potential temperature equation given below:

$$\frac{\partial \theta}{\partial t} = -u \frac{\partial \theta}{r \cos \phi \partial \lambda} - v \frac{\partial \theta}{r \partial \phi} - \omega \frac{\partial \theta}{\partial p} + (c_p \Pi)^{-1} Q_1$$

where  $r$  is Earth's radius,  $\phi$  is latitude,  $\lambda$  is longitude,  $c_p$  is specific heat capacity at constant pressure, and  $\Pi$  is the reduced Exner pressure, a diagnostic vertical velocity can be determined as made by *Hoppe et al.* [2016], assuming the temporal derivative is negligible at seasonal time scale. This leads to:

$$\omega_\theta = \frac{(c_p \Pi)^{-1} Q_1 - u \frac{\partial \theta}{r \cos \phi \partial \lambda} - v \frac{\partial \theta}{r \partial \phi}}{\frac{\partial \theta}{\partial p}} + res$$

where  $res$  is a residual due to sampling errors and budget approximations.

$\omega_\theta$  results from the contribution from the total heating and horizontal advection of temperature. Here we only consider the diabatic stream function linked to  $Q_1$  so that we neglect the horizontal derivative. This is equivalent to the Weak Temperature Gradient assumption (WTG) [*Sobel and Bretherton, 2000*] with a zero adjustment time since we consider monthly data. The obtained pressure velocity  $\omega_{diab}$  is given simply by:

$$\omega_{diab} = \frac{(c_p \Pi)^{-1} Q_1}{\partial \theta / \partial p}$$

To be consistent with assumptions made in the WTG approach, which does not apply in the boundary layer, a linear decrease of  $\omega_{diab}$  toward zero is applied below a constant boundary layer height, fixed here to 800 hPa [see *Daleu et al., 2016* for details]. Note that different nominal PBL heights have been tested for the computation of  $\omega_{diab}$  (from  $P_{pbl} = 925$  to 750 hPa); the results are rather insensitive to that choice. Note also that separate contributions from zonal and meridional advection could be computed but are beyond the scope of the study.

It is not expected for  $\omega_{diab}$  to perfectly capture the omega pattern over the (30°S–40°N) since meridional gradients temperature are significant in the vicinity of the SHL and submonthly transients may also alter the vertical velocity. The estimate of  $\omega_{diab}$  provides a simple view of the vertical velocity associated with the heating that can be modified by the horizontal dynamics (if meridional gradients of temperature are significant) or not.

Figure A1 shows the pressure velocity together with the “diabatic” pressure velocity. For all CMIP5 and prototype-CMIP6 versions of models or reanalysis, the deep ascent associated with deep convection is well depicted by the assumption. The large-scale subsidence over the ocean is also reproduced even though the location of the maximum subsidence is not really well located. However, the extent of the subsidence area and the general pattern is well handled by the diagnosed pressure velocity. The features of  $\omega_{diab}$  between 10°N and 25°N are less reliable as meridional gradients of temperature are significant there. Subsidence is found just north of the ITCZ for each model, corresponding to the downdraft cooling described in section 3.

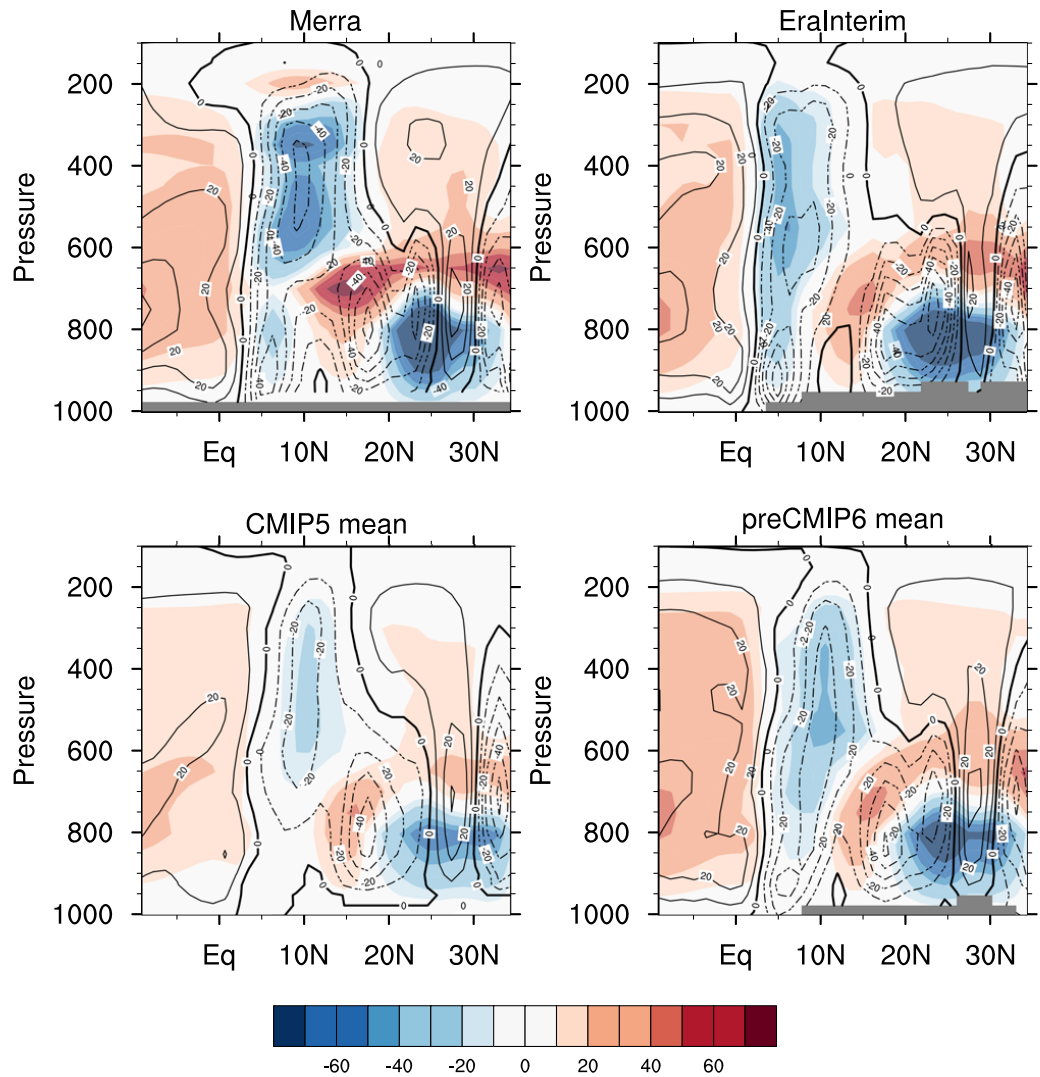


**Figure A1.** Meridional cross section of (10°W–10°E) mean diabatic pressure velocity,  $\omega_{diab}$  ( $\text{hPa d}^{-1}$ , colored shading), and the mean pressure velocity,  $\omega$  ( $\text{hPa d}^{-1}$ , contours every 10  $\text{hPa d}^{-1}$ , negative contours dotted), for JJA, in the two reanalyses and averaged over the CMIP5 and prototype-CMIP6 model simulations.

The shallow ascent associated with the SHL is placed more to the north, where the PBL heating is the greater which indicates that the observed ascent within the SHL is also driven by meridional gradient of temperature/pressure. Above it, the prevailing subsidence over the Sahara is well reproduced by  $\omega_{diab}$  too.

The monsoon circulation is analyzed using the zonal mean mass stream function,  $\bar{\psi}$  defined by:

$$\bar{\psi}(\phi, p) = \frac{2\pi a \cos(\phi)}{g} \int_{P_{top}}^p \overline{v(\lambda, \phi, p')} dp' \quad (1)$$

where  $a$  is the Earth's radius,  $g$  the acceleration due to gravity,  $v$  is the meridional wind and the overbar denotes a 10°W–10°E zonal average. Here equation (1) is integrated over atmospheric pressure levels ( $p$ ) from top to bottom assuming zero mass transport at 50 hPa [e.g., Trenberth et al. 2000]. Usually, this stream function is used for the global zonal average, for which the zonal divergence term vanishes, and describes accurately the meridional-vertical circulation. It is, however, an interesting synthetic variable also for regional purposes, with the restriction that integrating the meridional wind to derive  $\bar{\psi}$  does not give an accurate estimate of the true meridional-vertical circulation since the meridional wind is not fully nondivergent in the meridional-vertical [see Peyrillé et al., 2016].

To allow a proper use of equation (1), we use mass conservation in the meridional-vertical plane to determine a nondivergent meridional wind,  $\overline{v^{nd}}$ :

$$\overline{v^{nd}}(\phi, p) = \frac{a}{\cos(\phi)} \int_{30S}^{\phi} \cos(\phi') \frac{\partial \omega(\phi', p)}{\partial p} d\phi' \quad \text{with } \overline{v^{nd}}(\phi=30S, p)=0. \quad (2)$$

The pressure velocities  $\omega$  and  $\omega_{diab}$  can be used together with equation (2) to determine the corresponding nondivergent winds  $\overline{v^{nd}}$  and  $\overline{v_{diab}^{nd}}$ , which can then be introduced in equation (1) to determine the (10°W–10°E) mean nondivergent meridional stream function  $\overline{\psi^{nd}}$  and  $\overline{\psi_{diab}^{nd}}$ .

### Appendix B: Comparison Between the Zonal Mean Meridional Wind and Nondivergent Meridional Wind

Figure B1 displays the (10°W–10°E) zonal mean meridional wind  $\overline{v}$  compared with the nondivergent wind in the meridional-vertical plane,  $\overline{v^{nd}}$ . Note that  $(\overline{v^{nd}}, \omega)$  satisfies mass continuity in that plane. Peyrillé *et al.* [2016] used NCEP2 data for the same calculation. They found that the WAM structure is well-depicted by  $\overline{v^{nd}}$  except that West Africa is characterized by a domain-averaged large-scale subsidence and that the

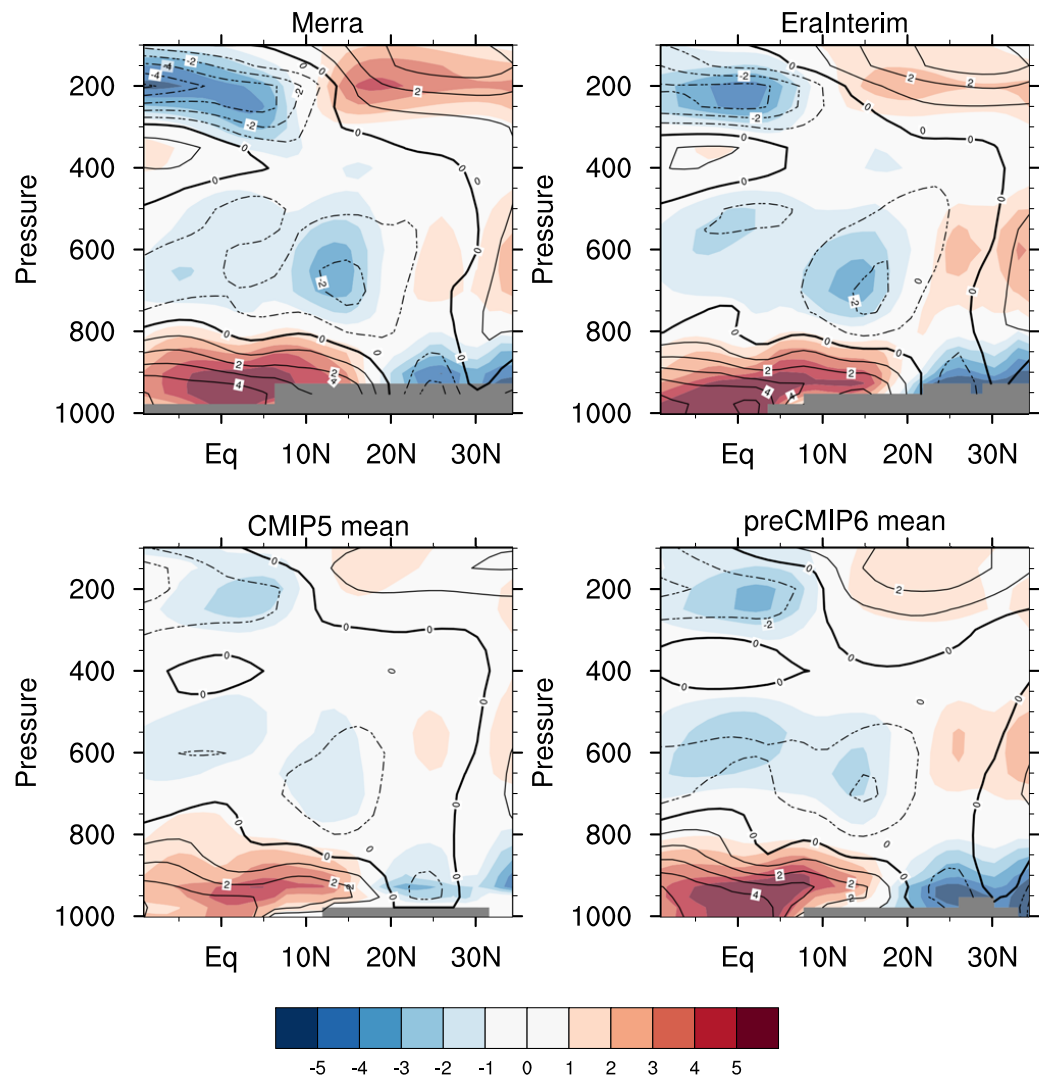


**Figure B1.** Meridional cross section of the (10°W–10°E) mean nondivergent meridional wind  $\overline{v^{nd}}$  ( $\text{m s}^{-1}$ , colors), defined as  $\overline{v^{nd}}(\phi, p) = \frac{a}{\cos(\phi)} \int_{30S}^{\phi} \cos(\phi') \frac{\partial \omega(\phi', p)}{\partial p} d\phi'$ , and the (10°W–10°E) mean meridional wind  $\overline{v}$  ( $\text{m s}^{-1}$ , contours at same interval as color scale, negative contours dotted), for JJA, in the two reanalyses and averaged over the CMIP5 and prototype-CMIP6 model simulations.

monsoon flow is overestimated. This calculation has been made for each model and reanalysis. For ERA-Interim and MERRA, the general pattern of the meridional circulation found with  $\overline{v^{nd}}$  is in good agreement with  $\overline{v}$ . Consistent with *Peyrillé et al.* [2016], there is too strong a monsoon flow when determined by  $\overline{v^{nd}}$  and a too intense southern branch of the deep meridional circulation. Note that an overestimate of the northern branch of the regional Hadley cell is found in both reanalysis but with a good location of the upper level divergence ( $\overline{v}=0$ ).

In the CMIP5 and prototype-CMIP6 models, the general pattern of the meridional wind matches between the two variables, especially in the lower troposphere where the transition from the monsoon flow to the Harmattan is well located. As analyzed by *Peyrillé et al.* [2016], the nondivergent wind tends to overestimate the monsoon flow and locates the maximum wind too far to the north ( $5\text{--}7\text{ m s}^{-1}$  for  $\overline{v^{nd}}$  versus  $3\text{--}4\text{ m s}^{-1}$  for  $\overline{v}$ ). The return flow at 700 hPa is rather well captured, though overestimated. In the upper troposphere, the poleward winds are overestimated in the vicinity of the upper level divergence ( $10^\circ\text{N}$ ) showing a not large enough meridional cell in both CMIP5 and prototype-CMIP6 versions. In summary, the general structure of the  $10^\circ\text{W}\text{--}10^\circ\text{E}$  averaged meridional wind is well captured by  $\overline{v^{nd}}$ .

### Appendix C: Calculation of Vertically Integrated Diabatic Components

In section 4.3, column-integrated budgets are considered for  $Q_1$ ,  $Q_2$ , and  $Q_1\text{--}Q_2$ . The budget equations of column-integrated  $Q_1$ ,  $Q_2$ , and  $h$  (the moist static energy) are:

1.  $\langle Q_1 \rangle = \langle Q_R \rangle + \langle Q_{1\text{CONV}} \rangle + \langle Q_{1\text{LS COND}} \rangle + \langle Q_{1\text{PBL}} \rangle$
2.  $\langle Q_2 \rangle = \langle Q_{2\text{CONV}} \rangle + \langle Q_{2\text{LS COND}} \rangle + \langle Q_{2\text{PBL}} \rangle$
3.  $\langle \dot{h}_{diab} \rangle = \langle Q_R \rangle + LE + H \equiv \langle Q_1 - Q_2 \rangle$

where the dot indicates a time derivative, the subscripts *R*, *CONV*, *LS COND*, and *PBL* stand for the heating/moistening produced by the radiation, convection, large-scale condensation and boundary layer parameterizations, and *H* and *LE* are the surface sensible and latent heating respectively. Note also that  $\langle Q_1\text{--}Q_2 \rangle$  stands for the production/consumption of column moist static energy by diabatic processes ( $\langle \dot{h}_{diab} \rangle$  in equation (3)) and that equations (1–3) are given in  $\text{W m}^{-2}$ . The angle brackets indicate mass-weighted vertical integration over the [1000–100 hPa] layer:

$$\langle (\cdot) \rangle \equiv \frac{1}{g} \int_{p_t}^{p_0} (\cdot) dp$$

where  $p_t$  is pressure at nominal constant tropopause ( $p_t = 100\text{ hPa}$ ) and  $p_0$  is 1000 hPa over the ocean and the first pressure level above orography over the continent.

#### Acknowledgments

This work was funded by the European Commission's 7th Framework Programme, under grant 282672, EMBRACE project. The authors acknowledge the contribution of F. Cheruy to the improvement of the soil model and the preparation of the LMDZ NPv4.12 simulations. The source codes for the new configurations of the models used in this study are not freely available as each represents a prototype configuration. However, comprehensive documentation is given in the supporting information and any further details can be obtained from the authors. The data used are archived and curated at the Met Office and can be obtained for research purposes from [gill.martin@metoffice.gov.uk](mailto:gill.martin@metoffice.gov.uk).

#### References

- Abel, S. J., and B. J. Shipway (2007), A comparison of cloud-resolving model simulations of trade wind cumulus with aircraft observations taken during RICO, *Q. J. R. Meteorol. Soc.*, *133*, 781–794, doi:10.1002/qj.55.
- Abel, S. J., and I. A. Boutle (2012), An improved representation of the raindrop size distribution for single-moment microphysics schemes, *Q. J. R. Meteorol. Soc.*, *138*, 2151–2162, doi:10.1002/qj.1949.
- Balsamo, G., S. Boussetta, E. Dutra, A. Beljaars, P. Viterbo, and B. V. den Hurk (2011), Evolution of land surface processes in the IFS, *ECMWF Newsl.*, *127*, 17–22.
- Bechtold, P., N. Semane, P. Lopez, J.-P. Chaboureaud, A. Beljaars, and N. Bormann (2014), Representing equilibrium and non-equilibrium convection in large-scale models, *J. Atmos. Sci.*, *71*, 734–753, doi:10.1175/JAS-D-13-0163.1.
- Belamari, S., and A. Pirani (2007), Validation of the optimal heat and momentum fluxes using the ORCA2-LIM global ocean-ice model, *Deliverable D4.1.3*, 88 pp., Marine Environment and Security for the European Area Integrated Project (MERSEA IP).
- Bellouin, N., J. Rae, A. Jones, C. Johnson, J. Haywood, and O. Boucher (2011), Aerosol forcing in the Climate Model Intercomparison Project (CMIP5) simulations by HadGEM2-ES and the role of ammonium nitrate, *J. Geophys. Res.*, *116*, D20206, doi:10.1029/2011JD016074.
- Best, M. J., et al. (2011), The Joint UK Land Environment Simulator (JULES), model description—Part 1: Energy and water fluxes, *Geosci. Model Dev.*, *4*, 677–699, doi:10.5194/gmd-4-677-2011.
- Bodas-Salcedo, A., K. D. Williams, P. R. Field, and A. P. Lock (2012), The surface downwelling solar radiation surplus over the Southern Ocean in the Met Office Model: The role of midlatitude cyclone clouds, *J. Clim.*, *25*, 7467–7486, doi:10.1175/JCLI-D-11-00702.1.
- Bony, S., and K. A. Emanuel (2001), A parameterization of the cloudiness associated with cumulus convection: Evaluation using TOGA COARE data, *J. Atmos. Sci.*, *58*, 3158–3183, doi:10.1175/1520-0469(2001)058<3158:APOTCA>2.0.CO;2.
- Boucher, O., and M. Pham (2002), History of sulfate aerosol radiative forcings, *Geophys. Res. Lett.*, *29*(9), 1308, doi:10.1029/2001GL014048.
- Bougeault, P., and P. Lacarrère (1989), Parameterization of orography-induced turbulence in a mesobeta-scale model, *Mon. Weather Rev.*, *117*, 1872–1890, doi:10.1175/1520-0493(1989)117<1872:POOITI>2.0.CO;2.

- Boutle, I. A., J. E. J. Eyre, and A. P. Lock (2014), Seamless stratocumulus simulation across the turbulent gray zone, *Mon. Weather Rev.*, *142*, 1655–1668, doi:10.1175/MWR-D-13-00229.1.
- Bush, S. J., A. G. Turner, S. J. Woolnough, G. M. Martin, and N. P. Klingaman (2015), The effect of increased convective entrainment on Asian monsoon biases in the MetUM general circulation model, *Q. J. R. Meteorol. Soc.*, *141*, 311–326, doi:10.1002/qj.2371.
- Caniaux, G., H. Giordani, J.-L. Redelsperger, F. Guichard, E. Key, and M. Wade (2011), Coupling between the Atlantic cold tongue and the West African monsoon in boreal spring and summer, *J. Geophys. Res.*, *116*, C04003, doi:10.1029/2010JC006570.
- Chadwick, R. C., G. M. Martin, D. Copesey, G. Bellon, M. Caian, F. Codron, C. Rio, and R. Roehrig (2017), Examining the West African monsoon circulation response to atmospheric heating in a GCM dynamical core, *J. Adv. Model. Earth Syst.*, doi:10.1002/2016MS000728.
- Clark, D. B., and N. Gedney (2008), Representing the effects of subgrid variability of soil moisture on runoff generation in a land surface model, *J. Geophys. Res.*, *113*, D10111, doi:10.1029/2007JD008940.
- Clark, D. B., et al. (2011), The Joint UK Land Environment Simulator (JULES), model description—Part 2: Carbon fluxes and vegetation dynamics, *Geosci. Model Dev.*, *4*, 701–722, doi:10.5194/gmd-4-701-2011.
- Couvreux, F., et al. (2015), Representation of daytime moist convection over the semi-arid Tropics by parametrizations used in climate and meteorological models, *Q. J. R. Meteorol. Soc.*, *141*, 2220–2236, doi:10.1002/qj.2517.
- Cusack, S., J. M. Edwards, and R. Kershaw (1999), Estimating the subgrid variance of saturation, and its parametrization for use in a gcm cloud scheme, *Q. J. R. Meteorol. Soc.*, *125*, 3057–3076, doi:10.1002/qj.49712556013.
- Cuxart, J., P. Bougeault, and J.-L. Redelsperger (2000), A turbulence scheme allowing for mesoscale and large-eddy simulations, *Q. J. R. Meteorol. Soc.*, *126*, 1–30, doi:10.1002/qj.49712656202.
- Daleu, C. L., et al. (2016), Intercomparison of methods of coupling between convection and large-scale circulation. 1: Comparison over uniform surface conditions, *J. Adv. Model. Earth Syst.*, *7*, 1576–1601, doi:10.1002/2015MS000468.
- Davies, T., M. J. P. Cullen, A. J. Malcolm, M. H. Mawson, A. Staniforth, A. A. White, and N. Wood (2005), A new dynamical core for the Met Office's global and regional modelling of the atmosphere, *Q. J. R. Meteorol. Soc.*, *131*, 1759–1782, doi:10.1256/qj.04.101.
- De Rosnay, P., J. Polcher, M. Bruen, and K. Laval (2002), Impact of a physically based soil water flow and soil-plant interaction representation for modeling large-scale land surface processes, *J. Geophys. Res.*, *107*(D11), 4118, doi:10.1029/2001JD000634.
- Derbyshire, S. H., A. V. Maidens, S. F. Milton, R. A. Stratton, and M. R. Willett (2011), Adaptive detrainment in a convective parametrization, *Q. J. R. Meteorol. Soc.*, *137*, 1856–1871, doi:10.1002/qj.875.
- Dharssi, I., P. Vidale, A. Verhoef, B. Macpherson, C. Jones, and M. Best (2008), New soil physical properties implemented in the Unified Model at PS18, *Tech. Rep. 528*, Meteorol. Res. and Dev., Met Off., Exeter, U. K. [Available at <http://www.metoffice.gov.uk/learning/library/publications/science/weather-science>.]
- Ducoudre, N., K. Laval, and A. Perrier (1993), SECHIBA, a new set of parametrizations of the hydrologic exchanges at the land/atmosphere interface within the LMD atmospheric general circulation model, *J. Clim.*, *6*(2), 248–273, doi:10.1175/1520-0442(1993)006<0248:SAN-SOP>2.0.CO;2.
- Edwards, J. M., and A. Slingo (1996), Studies with a flexible new radiation code. I: Choosing a configuration for a large-scale model, *Q. J. R. Meteorol. Soc.*, *122*, 689–719, doi:10.1002/qj.49712253107.
- Emanuel, K. A. (1991), A scheme for representing cumulus convection in large-scale models, *J. Atmos. Sci.*, *48*, 2313–2335, doi:10.1175/1520-0469(1991)048<2313:ASFRCC>2.0.CO;2.
- Essery, R., M. Best, and P. Cox (2001), MOSES 2.2 technical documentation, *Tech. Note 30*, 30 pp., Hadley Cent., Met Off., Berks, U. K. [Available at <http://library.metoffice.gov.uk/M10326UK/OPAC/Search/AdvancedSearch.aspx>.]
- FAO/IIASA/ISRIC/ISSCAS/JRC (2008), *Harmonized World Soil Database (version 1.0)*, FAO, Rome, Italy and IIASA, Laxenburg, Austria [Available at <http://webarchive.iiasa.ac.at/Research/LUC/External-World-soil-database/HTML/index.html>.]
- Fouquart, Y., and B. Bonnel (1980), Computations of solar heating of the earth's atmosphere: A new parameterization, *Beitr. Phys. Atmos.*, *53*, 35–62.
- García-Carreras, L., et al. (2014), The turbulent structure and diurnal growth of the Saharan atmospheric boundary layer, *J. Atmos. Sci.*, *72*(2), 693–713, doi:10.1175/JAS-D-13-0384.1.
- Grandpeix, J.-Y., and J.-P. Lafore (2010), A density current parameterization coupled with Emanuel's convection scheme. Part I: The models, *J. Atmos. Sci.*, *67*, 881–897, doi:10.1175/2009JAS3044.1.
- Grandpeix, J.-Y., V. Phillips, and R. Tailleux (2004), Improved mixing representation in Emanuel's convection scheme, *Q. J. R. Meteorol. Soc.*, *130*, 3207–3222, doi:10.1256/qj.03.144.
- Grandpeix, J.-Y., J.-P. Lafore, and F. Cheruy (2010), A density current parameterization coupled with Emanuel's convection scheme. Part II: 1D simulations, *J. Atmos. Sci.*, *67*, 898–922, doi:10.1175/2009JAS3045.1.
- Grant, A. L. M. (2001), Cloud-base fluxes in the cumulus-capped boundary layer, *Q. J. R. Meteorol. Soc.*, *127*, 407–421, doi:10.1002/qj.49712757209.
- Grant, A. L. M., and A. R. Brown (1999), A similarity hypothesis for shallow-cumulus transports, *Q. J. R. Meteorol. Soc.*, *125*, 1913–1936, doi:10.1002/qj.49712555802.
- Gregory, D., and P. R. Rowntree (1990), A mass flux convection scheme with representation of cloud ensemble characteristics and stability dependent closure, *Mon. Weather Rev.*, *118*, 1483–1506, doi:10.1175/1520-0493(1990)118<1483:AMFCSW>2.0.CO;2.
- Gregory, D., R. Kershaw, and P. M. Inness (1997), Parametrization of momentum transports by convection. II: Tests in single-column and general circulation models, *Q. J. R. Meteorol. Soc.*, *123*, 1153–1183, doi:10.1002/qj.49712354103.
- Guérémy, J. F. (2011), A continuous buoyancy based convection scheme: One- and three-dimensional validation, *Tellus, Ser. A*, *63*, 687–706, doi:10.1111/j.1600-0870.2011.00521.x.
- Hagos, S., and C. Zhang (2010), Diabatic heating, divergent circulation and moisture transport in the African monsoon system, *Q. J. R. Meteorol. Soc.*, *136*, 411–425, doi:10.1002/qj.538.
- Hazeleger, W., et al. (2012), EC-Earth V2.2: Description and validation of a new seamless earth system prediction model, *Clim. Dyn.*, *39*, 2611–2629, doi:10.1007/s00382-011-1228-5.
- Hill, P. G., J. Manners, and J. C. Petch (2011), Reducing noise associated with the Monte Carlo Independent Column Approximation for weather forecasting models, *Q. J. R. Meteorol. Soc.*, *137*, 219–228, doi:10.1002/qj.732.
- Hines, C. O. (1997), Doppler spread parameterization of gravity wave momentum deposition in the middle atmosphere. Part 2: Broad and quasi-monochromatic spectra and implementation, *J. Atmos. Sol. Terr. Phys.*, *59*, 387–400, doi:10.1016/S1364-6826(96)00080-6.
- Hoppe, C. M., F. Ploeger, P. Konopka, and R. Müller (2016), Kinematic and diabatic vertical velocity climatologies from a chemistry climate model, *Atmos. Chem. Phys.*, *16*, 6223–6239, doi:10.5194/acp-16-6223-2016.
- Hoskins, B. J., and M. J. Rodwell (1995), A model of the Asian summer monsoon. Part I: The global scale, *J. Atmos. Sci.*, *52*(9), 1329–1340, doi:10.1175/1520-0469(1995)052<1329:AMOTAS>2.0.CO;2.

- Hourdin, F., et al. (2010), AMMA-Model Intercomparison Project, *Bull. Am. Meteorol. Soc.*, *91*, 95–104, doi:10.1175/2009BAMS2791.1.
- Hourdin, F., et al. (2013a), Impact of the LMDZ atmospheric grid configuration on the climate and sensitivity of the IPSL-CM5A coupled model, *Clim. Dyn.*, *40*, 2167–2192, doi:10.1007/s00382-012-1411-3.
- Hourdin, F., et al. (2013b), LMDZ5B: The atmospheric component of the IPSL climate model with revisited parameterizations for clouds and convection, *Clim. Dyn.*, *40*, 2193–2222, doi:10.1007/s00382-012-1343-y.
- Huffman, G. J., R. F. Adler, M. Morrissey, D. Bolvin, S. Curtis, R. Joyce, B. McGavock, and J. Susskind (2001), Global precipitation at one-degree daily resolution from multi-satellite observations, *J. Hydrometeorol.*, *2*, 36–50, doi:10.1175/1525-7541(2001)002 < 0036:GPAODD>2.0.CO;2.
- Huffman, G. J., et al. (2007), The TRMM Multisatellite Precipitation Analysis (TMPA): Quasi-global, multiyear, combined-sensor precipitation estimates at fine scales, *J. Hydrometeorol.*, *8*, 38–55, doi:10.1175/JHM560.1.
- Kim, H.-K., and S. Lee (2001), Hadley cell dynamics in a primitive equation model. Part I: Axisymmetric flow, *J. Atmos. Sci.*, *58*, 2845–2858, doi:10.1175/1520-0469(2001)058 < 2845:HCDIAP>2.0.CO;2.
- Lafore, J.-P., C. Flamant, V. Giraud, F. Guichard, P. Knippertz, J.-F. Mahfouf, P. Mascart, and E. Williams (2010), Introduction to the AMMA Special issue on “Advances in understanding atmospheric processes over West Africa through the AMMA field campaign”, *Q. J. R. Meteorol. Soc.*, *136*, 2–7, doi:10.1002/qj.583.
- Lafore, J.-P., et al. (2011), Progress in understanding of weather systems in West Africa, *Atmos. Sci. Lett.*, *12*, 7–12, doi:10.1002/asl.335.
- Lappen, C.-L., and C. Schumacher (2012), Heating in the tropical atmosphere: What level of details is critical for accurate MJO simulations in GCMs?, *Clim. Dyn.*, *39*, 2547–2568, doi:10.1007/s00382-012-1327-y.
- Lau, K.-M., and L. Peng (1987), Origin of low-frequency (intraseasonal) oscillations in the tropical atmosphere. Part I: Basic theory, *J. Atmos. Sci.*, *44*, 950–972, doi:10.1175/1520-0469(1987)044 < 0950:OOLFOL>2.0.CO;2.
- Lin, H. (2009), Global extratropical response to diabatic heating variability of the Asian summer monsoon, *J. Atmos. Sci.*, *66*, 2697–2713, doi:10.1175/2009JAS3008.1.
- Lock, A. P., A. R. Brown, M. R. Bush, G. M. Martin, and R. N. B. Smith (2000), A new boundary layer mixing scheme. Part I: Scheme description and SCM tests, *Mon. Weather Rev.*, *128*, 3187–3199, doi:10.1175/1520-0493(2000)128 < 3187:ANBLMS>2.0.CO;2.
- Loeb, N. G., B. A. Wielicki, D. R. Doelling, G. L. Smith, D. F. Keyes, S. Kato, N. Manalo-Smith, and T. Wong (2009), Toward optimal closure of the Earth’s top-of-atmosphere radiation budget, *J. Clim.*, *22*, 748–766, doi:10.1175/2008JCLI2637.1.
- Lopez, P. (2002), Implementation and validation of a new prognostic large-scale cloud and precipitation scheme for climate and data-assimilation purposes, *Q. J. R. Meteorol. Soc.*, *128*, 229–257, doi:10.1256/00359000260498879.
- Lott, F. (1999), Alleviation of stationary biases in a GCM through a mountain drag parametrization scheme and a simple representation of mountain lift forces, *Mon. Weather Rev.*, *127*, 788–801, doi:10.1175/1520-0493(1999)127 < 0788:AOSBIA>2.0.CO;2.
- Lott, F., and M. J. Miller (1997), A new subgrid-scale orographic drag parametrization: Its formulation and testing, *Q. J. R. Meteorol. Soc.*, *123*, 101–127, doi:10.1002/qj.49712353704.
- Louis, J.-F. (1979), A parametric model of vertical eddy fluxes in the atmosphere, *Boundary Layer Meteorol.*, *17*, 187–202, doi:10.1007/BF00117978.
- Masson, V., J.-L. Champeaux, C. Chauvin, C. Meriguet, and R. Lacaze (2003), A global database of land surface parameters at 1 km resolution for use in meteorological and climate models, *J. Clim.*, *16*, 1261–1282, doi:10.1175/1520-0442-16.9.1261.
- Martin, G. M. et al. (2011), HadGEM2 Development Team: The HadGEM2 family of Met Office Unified Model climate configurations, *Geosci. Model Dev.*, *4*, 723–757, doi:10.5194/gmd-4-723-2011.
- Mellor, G. L., and T. Yamada (1982), Development of a turbulence closure model for geophysical fluid problems, *Rev. Geophys.*, *20*(4), 851–875, doi:10.1029/RG020i004p00851.
- Mlawer, E. J., and S. Clough (1997), Shortwave and longwave enhancements in the rapid radiative transfer model, in *Proceedings of the 7th Atmospheric Radiation Measurement (ARM) Science Team Meeting, CONF-9603149*, U.S. Dep. of Energy, Washington, D. C. [Available at <http://www.arm.gov/publications/proceedings/conf07/title.stm/mlaw-97.pdf>].
- Mlawer, E. J., S. J. Taubman, P. D. Brown, M. J. Iacono, and S. A. Clough (1997), Radiative transfer for inhomogeneous atmospheres: RRTM, a validated correlated-k model for the longwave, *J. Geophys. Res.*, *102*, 16,663–16,682, doi:10.1029/97JD00237.
- Morcrette, C. J. (2012), Improvements to a prognostic cloud scheme through changes to its cloud erosion parametrization, *Atmos. Sci. Lett.*, *13*, 95–102, doi:10.1002/asl.374.
- Morcrette, J.-J. (1991), Radiation and cloud radiative properties in the European Center for Medium Range Weather Forecasts forecasting system, *J. Geophys. Res.*, *96*, 9121–9132, doi:10.1029/89JD01597.
- Morcrette, J.-J., H. W. Barker, J. N. S. Cole, M. J. Iacono, and R. Pincus (2008), Impact of a new radiation package, McRad, in the ECMWF integrated forecasting system, *Mon. Weather Rev.*, *136*, 4773–4798, doi:10.1175/2008MWR2363.1.
- Nabat, P., et al. (2013), A 4-D climatology (1979–2009) of the monthly tropospheric aerosol optical depth distribution over the Mediterranean region from a comparative evaluation and blending of remote sensing and model products, *Atmos. Meas. Tech.*, *6*, 1287–1314, doi:10.5194/amt-6-1287-2013.
- Oki, T., and Y. D. Sud (1998), Design of Total Runoff Integrating Pathways (TRIP)—A global river channel network, *Earth Interact.*, *2*, 1–36, doi:10.1175/1087-3562(1998)002 < 0001:DOTRIP>2.3.CO;2.
- Peyrillé, P., J.-P. Lafore, and A. Boone (2016), The annual cycle of the West African monsoon in a two-dimensional model: Mechanisms of the rain-band migration, *Q. J. R. Meteorol. Soc.*, *142*, 1473–1489, doi:10.1002/qj.2750.
- Piriou, J.-M., J.-L. Redelsperger, J.-F. Geleyn, J.-P. Lafore, and F. Guichard (2007), An approach for convective parameterization with memory: Separating microphysics and transport in grid-scale equations, *J. Atmos. Sci.*, *64*(11), 4127–4139, doi:10.1175/2007JAS2144.1.
- Poan, D. E., R. Roehrig, F. Couvreux, and J.-P. Lafore (2013), West Africa Intraseasonal variability: A precipitable water perspective, *J. Atmos. Sci.*, *70*(4), 1035–1052, doi:10.1175/JAS-D-12-087.1.
- Poan, D. E., J.-P. Lafore, R. Roehrig, and F. Couvreux (2014), Internal processes within the African Easterly Wave system, *Q. J. R. Meteorol. Soc.*, *114*, 1121–1136, doi:10.1002/qj.2420.
- Quaas, J., O. Boucher, and F. M. Breon (2004), Aerosol indirect effects in POLDER satellite data and the Laboratoire de Meteorologie Dynamique-Zoom (LMDZ) general circulation model, *J. Geophys. Res.*, *109*, D08205, doi:10.1029/2003JD004317.
- Redelsperger, J.-L., and J.-P. Lafore (1994), Non-hydrostatic simulations of a cold front observed during the FRONTS-87 experiment, *Q. J. R. Meteorol. Soc.*, *120*, 519–555, doi:10.1002/qj.49712051703.
- Redelsperger, J.-L., C. D. Thorncroft, A. Diedhiou, T. Lebel, D. J. Parker, and J. Polcher (2006), African Monsoon Multidisciplinary Analysis: An international research project and field campaign, *Bull. Am. Meteorol. Soc.*, *87*, 1739–1746, doi:10.1175/BAMS-87-12-1739.
- Ricard, J. L., and J. F. Royer (1993), A statistical cloud scheme for use in an AGCM, *Ann. Geophys.*, *11*, 1095–1115.
- Rienecker, M. M., et al. (2011), MERRA: NASA’s Modern-Era retrospective analysis for research and Applications, *J. Clim.*, *24*, 3624–3648, doi:10.1175/JCLI-D-11-00015.1.

- Rio, C., and F. Hourdin (2008), A thermal plume model for the convective boundary layer: Representation of cumulus clouds, *J. Atmos. Sci.*, *65*, 407–425, doi:10.1175/2007JAS2256.1.
- Rochetin, N., F. Couvreux, J.-Y. Grandpeix, and C. Rio (2014a), Deep convection triggering by boundary layer thermals. Part I: LES analysis and stochastic triggering formulation, *J. Atmos. Sci.*, *71*(2), 496–514, doi:10.1175/JAS-D-12-0336.1.
- Rochetin, N., J.-Y. Grandpeix, C. Rio, and F. Couvreux (2014b), Deep convection triggering by boundary layer thermals. Part II: Stochastic triggering parameterization for the LMDZ GCM, *J. Atmos. Sci.*, *71*(2), 515–538, doi:10.1175/JAS-D-12-0337.1.
- Roehrig, R., D. Bouniol, F. Guichard, F. Hourdin, and J.-L. Redelsperger (2013), The present and future of the West African Monsoon: A process-oriented assessment of CMIP5 Simulations along the AMMA transect, *J. Clim.*, *26*, 6471–6505, doi:10.1175/JCLI-D-12-00505.1.
- Rotstain, L., B. Ryan, and J. Katzfey (2000), A scheme for calculation of the liquid fraction in mixed-phase stratiform clouds in large-scale models, *Mon. Weather Rev.*, *128*, 1070–1088, doi:10.1175/1520-0493(2000)128 < 1070:ASFCOT > 2.0.CO;2.
- Sadourny, R. (1975a), Compressible model flows on the sphere, *J. Atmos. Sci.*, *32*, 2103–2110, doi:10.1175/1520-0469(1975)032 < 2103:CMFOTS > 2.0.CO;2.
- Sadourny, R. (1975b), The dynamics of finite-difference models of the shallow-water equations, *J. Atmos. Sci.*, *32*, 680–689, doi:10.1175/1520-0469(1975)032 < 0680:TDOFDM > 2.0.CO;2.
- Sanchez, C., K. D. Williams, G. Shutts, and M. Collins (2014), Impact of a Stochastic Kinetic Energy Backscatter scheme across time-scales and resolutions, *Q. J. R. Meteorol. Soc.*, *140*, 2625–2637, doi:10.1002/qj.2328.
- Scaife, A. A., N. Butchart, C. D. Warner, and R. Swinbank (2002), Impact of a spectral gravity wave parametrization on the stratosphere in the Met Office Unified Model, *J. Atmos. Sci.*, *59*, 1473–1489, doi:10.1175/1520-0469(2002)059 < 1473:IOASGW > 2.0.CO;2.
- Schumacher, C., R. A. Houze Jr., and I. Kraucunas (2004), The tropical dynamical response to latent heating estimates derived from the TRMM precipitation radar, *J. Atmos. Sci.*, *61*, 1341–1358, doi:10.1175/1520-0469(2004)061 < 1341:TTDRTL > 2.0.CO;2.
- Scinocca, J. F. (2003), An accurate spectral nonorographic gravity wave drag parameterization for general circulation models, *J. Atmos. Sci.*, *60*, 667–682, doi:10.1175/1520-0469(2003)060 < 0667:AASNGW > 2.0.CO;2.
- Simmons, A., S. Uppala, D. P. Dee, and S. Kobayashi (2007), ERA-Interim: New ECMWF reanalysis products from 1989 onwards, *ECMWF Newsl.*, *110*, 25–35.
- Smith, R. N. B. (1990), A scheme for predicting layer clouds and their water content in a general circulation model, *Q. J. R. Meteorol. Soc.*, *116*, 435–460, doi:10.1002/qj.49711649210.
- Smith, R. N. B. (1993), Experience and developments with the layer cloud and boundary layer mixing schemes in the UK Meteorological Office Unified Model, in *Proceedings of the ECMWF/GCSS Workshop on Parametrization of the Cloud-Topped Boundary Layer*, ECMWF, Reading, U. K., 8–11 June.
- Sobel, A. H., and C. S. Bretherton (2000), Modeling tropical precipitation in a single column, *J. Clim.*, *13*, 4378–4392, doi:10.1175/1520-0442(2000)013 < 4378:MTPIAS > 2.0.CO;2.
- Stachnik, J. P., C. Schumacher, and P. E. Ciesielski (2013), Total heating characteristics of the ISCCP tropical and subtropical cloud regimes, *J. Clim.*, *26*, 7097–7116, doi:10.1175/JCLI-D-12-00673.1.
- Sultan, B., and S. Janicot (2003), The West African monsoon dynamics. Part II: The 'preonset' and 'onset' of the summer monsoon, *J. Clim.*, *16*, 3407–3427, doi:10.1175/1520-0442(2003)016 < 3407:TWAMDP > 2.0.CO;2.
- Sundqvist, H. (1978), A parameterization scheme for non-convective condensation including prediction of cloud water content, *Q. J. R. Meteorol. Soc.*, *104*, 677–690, doi:10.1002/qj.49710444110.
- Sundqvist, H. (1988), Parameterization of condensation and associated clouds in models for weather prediction and general circulation simulation, in *Physically-Based Modelling and Simulation of Climate and Climatic Change*, edited by M. E. Schlesinger, pp. 433–461, Kluwer Acad., Dordrecht, Netherlands, doi:10.1007/978-94-009-3041-4\_10.
- Szopa, S., et al. (2012), Aerosol and Ozone changes as forcing for Climate Evolution between 1850 and 2100, *Clim. Dyn.*, *40*, 2223–2250, doi:10.1007/s00382-012-1408-y.
- Taylor, K. E., R. J. Stouffer, and G. A. Meehl (2012), An overview of CMIP5 and the experiment design, *Bull. Am. Meteorol. Soc.*, *93*(4), 485–498, doi:10.1175/BAMS-D-11-00094.1.
- Tegen, I., P. Hollrig, M. Chin, I. Fung, D. Jacob, and J. Penner (1997), Contribution of different aerosol species to the global aerosol extinction optical thickness: Estimates from model results, *J. Geophys. Res.*, *102*, 23,895–23,915, doi:10.1029/97JD01864.
- Thorncroft, C. D., and M. Blackburn (1999), Maintenance of the African easterly jet, *Q. J. R. Meteorol. Soc.*, *125*, 763–786, doi:10.1002/qj.49712555502.
- Thorncroft, C. D., H. Nguyen, C. Zhang, and P. Peyrillé (2011), Annual cycle of the West African monsoon: Regional circulations and associated water vapour transport, *Q. J. R. Meteorol. Soc.*, *137*, 129–147, doi:10.1002/qj.728.
- Tiedtke, M. (1989), A comprehensive mass flux scheme for cumulus parameterization in large-scale models, *Mon. Weather Rev.*, *117*, 1779–1800, doi:10.1175/1520-0493(1989)117 < 1779:ACMFSF > 2.0.CO;2.
- Tiedtke, M. (1993), Representation of clouds in large-scale models, *Mon. Weather Rev.*, *121*, 3040–3061, doi:10.1175/1520-0493(1993)121 < 3040:ROCILS > 2.0.CO;2.
- Trenberth, K. E., D. P. Stepaniak, and J. M. Caron (2000), The Global Monsoon as seen through the Divergent Atmospheric Circulation, *J. Clim.*, *13*, 3969–3993, doi:10.1175/1520-0442(2000)013 < 3969:TGMASST > 2.0.CO;2.
- van Genuchten, M. T. (1980), A closed-form equation for predicting the hydraulic conductivity of unsaturated soils, *Soil Sci. Soc. Am. J.*, *44*, 892–898, doi:10.2136/sssaj1980.03615995004400050002x.
- Voltaire, A., et al. (2011), The CNRM-CM5.1 global climate model: Description and basic evaluation, *Clim. Dyn.*, *40*, 2091–2121, doi:10.1007/s00382-011-1259-y.
- Vosper, S. B., H. Wells, and A. R. Brown (2009), Accounting for non-uniform static stability in orographic drag parametrization, *Q. J. R. Meteorol. Soc.*, *135*, 815–822, doi:10.1002/qj.407.
- Walters, D. N., et al. (2011), The Met Office Unified Model Global Atmosphere 3.0/3.1 and JULES Global Land 3.0/3.1 configurations, *Geosci. Model Dev.*, *4*, 919–941, doi:10.5194/gmd-4-919-2011.
- Walters, D. N., et al. (2014), The Met Office Unified Model Global Atmosphere 4.0 and JULES Global Land 4.0 configurations, *Geosci. Model Dev.*, *7*, 361–386, doi:10.5194/gmd-7-361-2014.
- Walters, D. N., et al. (2016), The Met Office Unified Model Global Atmosphere 6.0/6.1 and JULES Global Land 6.0/6.1 configurations, *Geosci. Model Dev. Discuss.*, doi:10.5194/gmd-2016-194, in review.
- Wilson, D. R., and S. P. Ballard (1999), A microphysically based precipitation scheme for the UK Meteorological Office Unified Model, *Q. J. R. Meteorol. Soc.*, *125*, 1607–1636, doi:10.1002/qj.49712555707.
- Wilson, D. R., A. C. Bushell, A. M. Kerr-Munslow, J. D. Price, and C. J. Morcrette (2008), PC2: A prognostic cloud fraction and condensation scheme. I: Scheme description, *Q. J. R. Meteorol. Soc.*, *134*, 2093–2107, doi:10.1002/qj.333.

- Wood, N., et al. (2013), An inherently mass-conserving semi-implicit semi-Lagrangian discretization of the deep-atmosphere global non-hydrostatic equations, *Q. J. R. Meteorol. Soc.*, *140*, 1505–1520, doi:10.1002/qj.2235.
- Woodward, S. (2011), Mineral dust in HadGEM2. *Hadley Centre Tech. Note 87*, Met. Off. Hadley Cent., Exeter, U. K. [Available at <http://www.metoffice.gov.uk/learning/library/publications/science/climate-science-technical-notes>.]
- Xie, P.P., and Arkin, P.A. (1997), Global Precipitation: A 17-year monthly analysis based on gauge observations, satellite estimates, and numerical model outputs, *Bull. Am. Meteorol. Soc.*, *78*, 2539–2558, doi:10.1175/1520-0477(1997)078<2539:GPAYMA>2.0.CO;2.
- Xue, Y., et al. (2010), Intercomparison and analyses of the climatology of the West African Monsoon in the West African Monsoon Modeling and Evaluation project (WAMME) first model intercomparison experiment, *Clim. Dyn.*, *35*, 3–28, doi:10.1007/s00382-010-0778-2.
- Yamada, T. (1983), Simulations of nocturnal drainage flows by a  $Q_2$  turbulence closure model, *J. Atmos. Sci.*, *40*, 91–106, doi:10.1175/1520-0469(1983)040<0091:SONDFB>2.0.CO;2.
- Yanai, M., S. Esbensen, and J.-H. Chu (1973), Determination of bulk properties of tropical cloud clusters from large-scale heat and moisture budgets, *J. Atmos. Sci.*, *30*, 611–627, doi:10.1175/1520-0469(1973)030<0611:DOBPOT>2.0.CO;2.
- Zender, C. S., and J. T. Kiehl (1997), Sensitivity of climate simulations to radiative effects of tropical anvil structure, *J. Geophys. Res.*, *102*, 23,793–23,803, doi:10.1029/97JD02009.
- Zhang, Y., and S. A. Klein (2013), Factors controlling the vertical extent of fair-weather shallow cumulus clouds over land: Investigation of diurnal-cycle observations collected at the ARM Southern Great Plains site, *J. Atmos. Sci.*, *70*, 1297–1315, doi:10.1175/JAS-D-12-0131.1.